AIMS Mathematics, 11(11): 38994–39039.
DOI:10.3934/math.20261503
Received: 18 September 2026
Revised: 30 October 2026
Accepted: 11 November 2026
Published: 23 November 2026

https://www.aimspress.com/journal/Math

Research article

Recruitment shape governs the bifurcation pattern of a semidiscrete pine nematode model

Mi Wang[1] **and Wenlong Song**[2,*]

[1] College of Science, Northeast Forestry University, Harbin 150040, China

[2] School of Computer Science and Artificial Intelligence, Northeast Forestry University, Harbin 150040, China

* **Correspondence:** Email: wlsong139@126.com.

Abstract: We apply the piecewise constant arguments method to construct a two-dimensional, semidiscrete map that describes the generational population dynamics of the pine wood nematode *Bursaphelenchus xylophilus* under a maturation delay, neglecting spatial diffusion. Two canonical density-dependent recruitment forms are compared: the Ricker function, which is hump-shaped and embodies overcompensatory density dependence, and the Beverton–Holt function, which is monotone increasing and saturates, embodying compensatory density dependence. For both maps, we establish the existence of a unique positive equilibrium and derive a complete Jury-type stability criterion. The Ricker equilibrium loses stability through a supercritical Neimark–Sacker bifurcation, giving rise to quasiperiodic oscillations, whereas a period-doubling bifurcation is structurally excluded. In the Beverton–Holt map, the Jacobian determinant is strictly negative at every positive equilibrium, so that a Neimark–Sacker bifurcation can never occur; the unique destabilization mechanism is a supercritical period-doubling bifurcation, and the positive equilibrium exchanges stability with the extinction state through a transcritical bifurcation when the basic reproduction number crosses one. Numerical simulations, including generational time series and parameter-dependent bifurcation diagrams, confirm all analytical predictions and show that chaotic dynamics are absent in both models. The comparison demonstrates that the recruitment function, rather than a modeling detail, dictates the type of instability and the shape of outbreaks and provides practical guidance for choosing between the two forms in pest management.

Keywords: pine wood nematode; semidiscrete model; Ricker and Beverton–Holt recruitment function; Neimark–Sacker bifurcation; period-doubling bifurcation
Mathematics Subject Classification: 37G15, 37N25, 39A28, 92D25

1. Introduction

The pine wood nematode *Bursaphelenchus xylophilus*, the causal agent of pine wilt disease, is one of the most destructive invasive forest pests in the world [1, 2]. Native to North America, it was introduced into Japan at the beginning of the twentieth century, was first detected in mainland China in Nanjing in 1982, and has since spread to 19 provinces and more than 700 county-level regions in China [3, 4]; it reached Portugal in 1999 and is regarded as a major threat to European pine forests [5]. An uncontrolled invasion in Europe has been estimated to cause a cumulative loss of coniferous timber of about 22 billion euros over the period 2008–2030 [6]. The nematode is transmitted from diseased to healthy trees mainly by longhorn beetles of the genus *Monochamus*: The beetle carries the nematode while feeding on the twigs of a healthy pine, the nematode invades the resin canals and kills the tree within a few months, and the next generation of beetles emerging from the dead tree carries a new nematode load to neighboring pines [2, 7]. Because this beetle–nematode transmission cycle together with the within-tree development of the nematode lasts about one year, the generational dynamics is naturally formulated as a delay model in which the current recruitment is produced by the population density one generation earlier [7,8]. Figure 1 shows the causal agent and the vector of pine wilt disease: the microscopic morphology of *B. xylophilus* and the longhorn beetle *Monochamus alternatus*, the principal vector of the disease in China.



(a) Bursaphelenchus xylophilus, light microscopy (b) Monochamus alternatus on a pine twig

Figure 1. The causal agent and the vector of pine wilt disease. (a) Light-microscopic photographs of *Bursaphelenchus xylophilus* from *Pinus sylvestris* in Portugal, showing the diagnostic characters of the male and the female; reprinted from [9] under the CC BY 4.0 license (`https://doi.org/10.3390/f15091556`). (b) The vector beetle *Monochamus alternatus* feeding on a pine twig; photograph courtesy of the Gengzhongbang Plantation Network (`http://www.gengzhongbang.com/article-12191-1.html`).

Figure 2 illustrates the typical field signature of the disease, in which wilted red-brown pines stand out against the healthy green forest.



Figure 2. Field symptoms of pine wilt disease in China: an infected pine with the whole crown killed (left) and a pine stand with contiguous dead trees (right). The characteristic red-brown wilted needles remain attached to the branches; photographs from the publicity material of the Pubei County Government, Guangxi, China (`http://www.gxpb.gov.cn/zfxxgk/zfbmgkpt/gzjd/btz/fdzdgknr_42/bmwj37/t15754409.shtml`).

The continuous model underlying this paper is taken from the age-structured forest-pest diffusive model proposed by [10] in the degenerate case $d = 0$, and its semidiscrete treatment follows the piecewise-constant-arguments framework [11]. Related stage-structured population models with maturation delays have also been investigated in [12]. Delay-induced oscillations in population dynamics have been studied since the early work of Nazarenko [13]. Let $w = w(x,t)$ denote the nematode load in the matured population; $\tau > 0$ the maturation time; δ and γ the death rates of the immature and mature individuals. respectively; and $d > 0$ the diffusion rate of the matured individuals. Then, the total matured population satisfies

$$\frac{\partial w}{\partial t} = d\Delta w - \gamma w - \frac{w^2}{1+w^2} + \mathrm{e}^{-\delta\tau} f(w(x,t-\tau)), \tag{1.1}$$

where $w^2/(1+w^2)$ is the Holling-type-III term describing the saturation of the vector-borne transmission and of the host resistance [14]; f is a general recruitment function, to be specified below; and $\mathrm{e}^{-\delta\tau}$ is the survival probability through the maturation period τ.

Figure 3 summarizes the bridge between the ecological cycle of the disease and the mathematical mechanism analyzed in this paper: The generational delay of the beetle–nematode cycle enters the continuous delay model, the semidiscrete map is built on the piecewise-constant-arguments discretization and the bifurcation mechanism of the outbreak separates the latent and the outbreak regimes at the threshold τ^*.

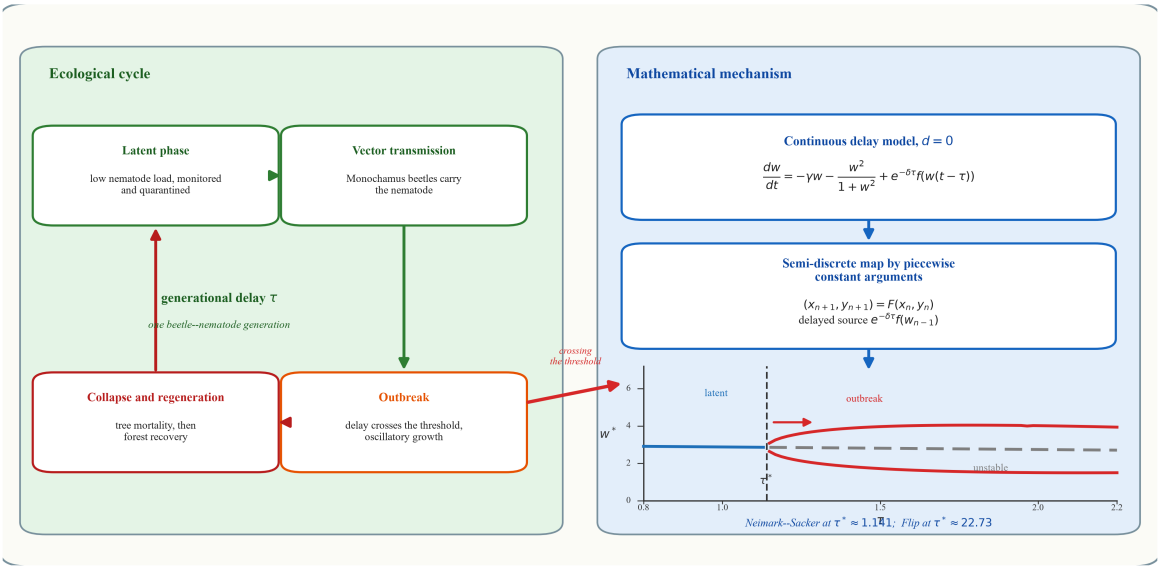

Figure 3. From the ecological cycle of pine wilt disease to the mathematical mechanism of the semidiscrete model. Left: the beetle–nematode generation cycle, in which the maturation delay τ equals one beetle-nematode generation; crossing the threshold drives the system from the latent phase into the outbreak phase. Right: the continuous delay model with $d = 0$, its semidiscrete map obtained by the piecewise-constant- arguments method, and the bifurcation mechanism of the outbreak, in which the stable, low-density branch, the unstable continuation, and the outbreak envelope are separated by the threshold τ^*. This bifurcation sketch is plotted for the Ricker recruitment function, for which the outbreak is destabilized by a supercritical Neimark–Sacker bifurcation at $\tau^* \approx 1.141$; the corresponding scenario for the Beverton–Holt recruitment function, a period-doubling bifurcation at $\tau^*_{\text{flip}} \approx 22.73$, is indicated for comparison.

Two canonical forms of the recruitment function are widely used in stock-recruitment and insect-outbreak modeling. The Ricker function [15] is hump-shaped and overcompensatory: Total recruitment first increases with density, attains a maximum, and then declines to zero so that at high density, the total recruitment falls. This overcompensatory shape describes populations in which density dependence acts so strongly at high density that the total number of recruits decreases, for example under strong cannibalism, egg limitation, or disease transmission intensified by crowding. Its main advantage is the ability to produce a collapse of recruitment at high density, regarded as an essential ingredient of the outbreak–crash cycles of many forest insects [10, 16], whereas its limitation is that this collapse and the associated strong destabilization occur only on the decreasing branch of the recruitment curve. The Beverton–Holt function [17] is strictly increasing, concave, and saturating: The per-capita recruitment declines smoothly with density (compensation), whereas the total recruitment remains bounded and never decreases. It is the classical stock-recruitment curve of fishery science and applies to populations in which density regulation is purely compensatory; its advantages are monotonicity, boundedness, and the transparent biological meaning of the saturation parameter a, whereas its limitation is that it cannot describe the overcompensatory collapse of recruitment. The explicit algebraic forms of these two functions are substituted in Section 3 and Section 4, respectively,

where their shapes are shown to determine the qualitative dynamics of the semidiscrete model. These two forms encode fundamentally different mechanisms of density regulation, and a central question of this paper is whether, and if so, how, the choice of the recruitment function qualitatively changes the equilibrium structure and the bifurcation structure of the semidiscrete delay model. As we shall see, the answer is emphatic: The Ricker model destabilizes through a supercritical Neimark–Sacker bifurcation (invariant closed curve, quasiperiodic oscillations) and admits no period-doubling, whereas the Beverton–Holt model excludes Neimark–Sacker bifurcations on purely structural grounds (its Jacobian determinant is always negative) and destabilizes instead through a supercritical period-doubling (Flip) bifurcation. In both models, chaotic dynamics is absent. A full comparison and biological guidance for the selection of the recruitment function are given in Section 5.

In this paper, we study the case without spatial diffusion ($d = 0$), in which case, (1.1) reduces to the single species-delayed differential equation [8, 18]

$$\frac{\mathrm{d}w}{\mathrm{d}t} = -\gamma w(t) - \frac{w(t)^2}{1 + w(t)^2} + \mathrm{e}^{-\delta\tau} f(w(t-\tau)). \tag{1.2}$$

In the practice of forestry engineering and pest management, every term of (1.2) carries a concrete operational meaning. The delay τ represents the beetle–nematode generation period; the mortality rates δ and γ are manipulated in the field through the removal of dead and dying pines through quarantine and heat treatment of infested wood and through the suppression of the vector beetle by trap trees, attractants, and biological control [1, 3, 4]. The analysis below attaches a precise prediction to each of these operations. For the Ricker model, the positive equilibrium is destabilized by a supercritical Neimark–Sacker bifurcation at a critical delay $\tau^* \approx 1.141$, after which, the outbreak oscillates quasi-periodically with an amplitude growing as $\sqrt{\tau - \tau^*}$; the corresponding recovery strategy is to keep the effective generation delay below τ^* by increasing the mortality of either stage, that is, the pair (δ, γ). For the Beverton–Holt model, the Jacobian determinant is strictly negative, and the unique destabilization is a supercritical period-doubling bifurcation so that the outbreak alternates between an outbreak year and a suppressed year; the recovery strategy is then to act on the saturation strength a of the recruitment. In both models, chaotic dynamics is absent, which legitimizes long-term prediction and makes the model output a reliable basis for management decisions. The regime shift between the latent phase and the outbreak phase and the two different bifurcation scenarios generated by the two recruitment forms are visualized in Section 5.

In recent years, the theory of difference equations has been widely applied to discrete systems in computer science, economics, ecology, and control theory, in particular, in population dynamics [19, 20]. Many authors [21,22] have argued that difference equation models are more appropriate than their continuous counterparts, especially when the population has nonoverlapping generations. For forest-pest models, the classical continuous model of [16] and its discrete versions have been extensively studied [23–26]; in particular, [26] recently investigated the pattern dynamics of a space–time discrete forest-pest model. However, how to discretize a delayed continuous model faithfully so as to preserve its fixed points, stability, and bifurcation structure remains a nontrivial question.

In this paper, we employ the piecewise constant arguments semidiscretization method of [11] to treat the delay in (1.2). This method, systematically developed by [27] and Wiener [28], has been successfully applied to various delayed population models [11, 29–31]; it occupies an intermediate position between differential and difference equations: On each interval, of length equal to the delay

τ, the delayed feedback is frozen at its left endpoint so that one obtains an autonomous scalar equation that can be integrated exactly, and hence, an explicit two-dimensional discrete map. Unlike the classical population model treated by [11] (whose birth term is proportional to the current population density), the birth term $e^{-\delta\tau} f(w(t-\tau))$ of our model (1.2) depends only on the delayed state $w(t-\tau)$ and is independent of the current state $w(t)$. This essential difference has a direct consequence: If one composes the birth term into a pure per-capita exponential factor as in paper, the semidiscrete map becomes unstable and diverges already at a very small delay (e.g., $\tau^* \approx 0.33$ under the parameters used below); hence, the delayed feedback must be treated as a constant source term and integrated exactly by the integrating-factor (exponential Euler) scheme. The resulting explicit, positivity-preserving semidiscrete scheme (denoted S2) reduces to the classical exponential map [11] when the predation term vanishes. This is the most essential difference from the semidiscretization method [11] and constitutes one of the main contributions of this paper.

The main goal of this paper is to investigate the dynamics of the S2 semidiscrete system of (1.2), obtained from the general form by the piecewise-constant-arguments semidiscretization described above; the complete derivation is carried out in Section 2, and no concrete form of the recruitment function f is needed at this stage,

$$\begin{cases} x(n+1) = y(n), & A_n = -\gamma\tau - \tau \dfrac{y(n)}{1+y(n)^2}, \\ y(n+1) = y(n)e^{A_n} + C_n \dfrac{e^{A_n}-1}{A_n}, & C_n = \tau\, e^{-\delta\tau} f(x(n)). \end{cases} \tag{1.3}$$

We prove that the dynamics of (1.3) is qualitatively consistent with that of the continuous model (1.2), yet the thresholds are shifted: The positive fixed point $E_+ = (w^*, w^*)$ is locally asymptotically stable for $\tau < \tau^* \approx 1.141$; when τ crosses τ^* , a supercritical Neimark–Sacker bifurcation occurs, and an asymptotically stable invariant, closed curve quasiperiodic oscillation) bifurcates from E_+, whose amplitude grows according to $\sqrt{\tau - \tau^*}$. As τ is further increased, the system exhibits more complicated quasiperiodic frequency-locked , and more complicated oscillatory behaviors. In the continuous model (1.2), such behaviors appear only at larger delays (Hopf thresholds $\tau_H^0 \approx 2.01$ and $\tau_H^1 \approx 4.45$). Thus, the piecewise-constant-arguments semidiscretization shifts the destabilization threshold significantly earlier, by about half, a noteworthy discretization effect.

The rest of this paper is organized as follows. Section 2 develops the piecewise-constant-arguments semidiscretization of [11] for a *general* recruitment function f, establishing the framework of fixed points, linearization, and the Jury criterion without committing to a particular recruitment form. Section 3 specializes this framework to the two recruitment functions, the Ricker and the Beverton–Holt forms, analyzing the stability, the bifurcation structure, and the absence of chaotic dynamics in each case. Section 4 presents numerical simulations supporting the theoretical results, with representative delay values for each model. Section 5 compares the two models and gives biological guidance on the choice of the recruitment function from an ecological perspective. Section 6 summarizes the paper.

2. Recruitment functions and the semidiscrete framework

The recruitment function f encodes the mechanism of density-dependent reproduction and is the single most important modeling decision in stock-recruitment and insect-outbreak dynamics [15,

17, 19]. The two canonical shapes adopted in this paper, the hump-shaped Ricker function and the saturating Beverton–Holt function, and their ecological advantages and limitations, have been discussed in the introduction. In this section, we keep the recruitment function f general and develop the semidscrete framework for an arbitrary f satisfying a few mild regularity assumptions: the normalization of the delay; the piecewise-constant-arguments discretization; and the generalized fixe-point, linearization, and Jury-type stability criteria. The concrete Ricker and Beverton–Holt forms are then substituted only in Section 3 and Section 4, where their shapes determine the qualitative dynamics.

2.1. General assumptions on the recruitment function

Throughout Section 2, the recruitment function f is kept unspecified and is assumed only to satisfy the mild structural conditions

$$f(0) = 0, \qquad f(w) > 0 \ \ (w > 0), \qquad f \in C^3[0, \infty) \tag{2.1}$$

so that no recruitment occurs at zero population density, recruitment is positive at any positive density, and the semidscrete map inherits sufficient smoothness for a rigorous bifurcation analysis. Two shapes of f will be of interest, and their qualitative difference is the subject of the whole paper:

- A hump-shaped (overcompensatory) recruitment function, for which the slope $f'(w)$ changes sign at some $w = w_{\max}$: Total recruitment increases for $w < w_{\max}$, attains a maximum, and then declines to zero so that at high density, the total number of recruits *decreases*;
- A strictly increasing, saturating (compensatory) recruitment function, for which $f'(w) > 0$ for all $w > 0$ and f remains bounded: Total recruitment increases monotonically toward a saturation level and never decreases.

These two shapes encode fundamentally different mechanisms of density regulation, and Sections 3 and 4 show that this difference is not a modeling detail: It determines the entire qualitative dynamics of the semidiscrete delay system. Mathematically, the shape of f enters the Jacobian of the semidiscrete map only through the slope $f'(w^*)$ at the fixed point, as shown below. For a hump-shaped function, the slope changes sign, so the Jacobian determinant may be positive or negative, and a Neimark–Sacker bifurcation becomes possible; for a strictly increasing function, $f'(w) > 0$ for all w . Hence, $\det J < 0$ identically, and a Neimark–Sacker bifurcation is structurally impossible so that the destabilization must then occur through a real multiplier, namely a period-doubling (Flip) bifurcation. In both cases, the maximal Lyapunov exponent remains nonpositive so chaotic dynamics is absent.

2.2. Normalization of the delay

Letting $s = t/\tau$ and writing $\eta(s) = w(\tau s) = w(t)$, we have $w(t - \tau) = \eta(s - 1)$ and $\dfrac{\mathrm{d}w}{\mathrm{d}t} = \dfrac{1}{\tau}\dfrac{\mathrm{d}\eta}{\mathrm{d}s}$. Hence, Eq (1.2) becomes

$$\frac{\mathrm{d}\eta}{\mathrm{d}s} = -\gamma\tau\,\eta(s) - \tau\frac{\eta(s)^2}{1 + \eta(s)^2} + \tau\,\mathrm{e}^{-\delta\tau} f(\eta(s - 1)), \qquad s \geq 1, \tag{2.2}$$

where f is a general recruitment function satisfying the structural conditions (2.1). Throughout this section, f is kept unspecified; the two concrete choices, the Ricker function and the Beverton–Holt function, are substituted only in Sections 3 and 4. Here, $\gamma\tau$, τ and $\tau\mathrm{e}^{-\delta\tau}$ correspond, respectively, to the

normalized parameters p and q of the normalized framework, that is, the average rate of change within one delay period τ in [11].

2.3. Piecewise constant arguments and exact integration

Following [11], we replace the delayed argument $\eta(s-1)$ in (2.2) by its integer part $\eta([s-1])$, that is, for every $n = 1, 2, \ldots$ and $s \in [n, n+1)$, $\eta(s-1) = \eta(n-1)$ is a constant. Then,

$$\frac{\mathrm{d}\eta}{\mathrm{d}s} = -\gamma\tau\,\eta(s) - \tau\frac{\eta(s)^2}{1+\eta(s)^2} + \tau\,\mathrm{e}^{-\delta\tau} f(\eta(n-1)), \qquad s \in [n, n+1). \tag{2.3}$$

On each interval, $[n, n+1)$ the delayed feedback is frozen as the constant source term

$$C_n := \tau\,\mathrm{e}^{-\delta\tau} f(\eta(n-1)). \tag{2.4}$$

Equation (2.3) is an autonomous scalar equation with a constant source term; its time-1 flow (one delay period τ on the original time scale) defines the semidiscrete map

$$\eta(n+1) = \Phi(\eta(n);\, C_n), \qquad \frac{\mathrm{d}\eta}{\mathrm{d}s} = -\gamma\tau\,\eta - \tau\frac{\eta^2}{1+\eta^2} + C_n \text{ at time 1.} \tag{2.5}$$

Because the predation term $\eta^2/(1+\eta^2)$ prevents (2.5) from being written in the closed exponential form of [11], we use in practice the integrating factor explicit scheme, which integrates the linear death part exactly and freezes the current-state density term

$$\eta(n+1) = \eta(n)\,\mathrm{e}^{A_n} + C_n\,\frac{\mathrm{e}^{A_n}-1}{A_n}, \qquad A_n := -\gamma\tau - \tau\,\frac{\eta(n)}{1+\eta(n)^2} < 0. \tag{2.6}$$

Scheme (2.6) preserves the exponential structure multiply by $\mathrm{e}^{(\cdot)}$ of the map [11], preserves positivity for positive initial data, and reduces to the classical exponential map when the predation term vanishes; when $A_n = 0$, it is understood in the limiting sense $\eta(n+1) = \eta(n) + C_n$.

Introducing as in [11]

$$x(n) = \eta(n-1), \qquad y(n) = \eta(n), \tag{2.7}$$

the semidiscrete model (2.6) is transformed into the two-dimensional map

$$\begin{cases} x(n+1) = y(n), & A_n = -\gamma\tau - \tau\dfrac{y(n)}{1+y(n)^2}, \\ y(n+1) = y(n)\,\mathrm{e}^{A_n} + C_n\,\dfrac{\mathrm{e}^{A_n}-1}{A_n}, & C_n = \tau\,\mathrm{e}^{-\delta\tau} f(x(n)). \end{cases} \tag{2.8}$$

This is the two-dimensional semidiscrete system isomorphic to the one in [11]; we denote the associated map by $F : \mathbb{R}^2 \to \mathbb{R}^2$.

Remark 2.1. *The essential difference from the model [11]: In* (2.8) *, the birth term C_n depends only on the delayed state $x(n) = \eta(n-1)$, whereas in the updating equation of $y(n)$ the term A_n depends only on the current state $y(n)$. If as in [11], one composed the birth term into the exponential (i.e., merged C_n into the exponential of A_n), the resulting map would become unstable and diverge at the very small delay $\tau^* \approx 0.33$ under the parameters $\gamma = 1,\ \delta = 0.1,\ b = 14.5,\ a = 0.8$; see the numerical comparison in Section 3.8. Hence, C_n must be treated as the source term* (2.4)*.*

2.4. Fixed points, linearization, and the Jury criterion

Let $E_+ = (w^*, w^*)$ be a positive fixed point of (2.8). From $x(n+1) = y(n)$, we obtain $x^* = y^* = w^*$, and w^* satisfies the generalized equilibrium equation

$$\gamma + \frac{w^*}{1 + w^{*2}} = \mathrm{e}^{-\delta\tau} f(w^*). \tag{2.9}$$

With $R_0 := \dfrac{\mathrm{e}^{-\delta\tau} f'(0)}{\gamma}$ the trivial fixed point $E_0 = (0, 0)$ always exists, and a positive fixed point can appear only when the net recruitment after the maturation period exceeds the loss rate, that is, when $R_0 > 1$; the precise existence and uniqueness statements depend on the shape of f and are established separately for the two recruitment functions in Sections 3 and 4.

Linearizing the exact flow about w^* and setting $z(n) = \eta(n) - w^*$, we obtain the linear semidiscrete equation

$$z(n+1) = \mathrm{e}^A z(n) + B \frac{\mathrm{e}^A - 1}{A} z(n-1), \tag{2.10}$$

where

$$A = -\gamma\tau - \frac{2\tau w^*}{(1 + w^{*2})^2}, \qquad B = \tau \mathrm{e}^{-\delta\tau} f'(w^*). \tag{2.11}$$

The corresponding characteristic equation of the two-dimensional linear map is

$$\lambda^2 - \mathrm{e}^A \lambda - B \frac{\mathrm{e}^A - 1}{A} = 0. \tag{2.12}$$

Thus, the entire linear stability problem of the semidiscrete model depends on the recruitment function only through the slope $f'(w^*)$ at the fixed point.

Write $P(\lambda) = \lambda^2 - \mathrm{e}^A \lambda - B\dfrac{\mathrm{e}^A - 1}{A}$ so that $P(1)$ and $P(-1)$ are the two boundary values entering the Jury test.

Lemma 2.2 (Generalized Jury criterion [11])**.** *Let $A < 0$, and $B = \tau \mathrm{e}^{-\delta\tau} f'(w^*)$. Then, E_+ is locally asymptotically stable if and only if*

$$P(1) = 1 - \mathrm{e}^A - B \frac{\mathrm{e}^A - 1}{A} > 0, \qquad P(-1) = 1 + \mathrm{e}^A - B \frac{\mathrm{e}^A - 1}{A} > 0, \qquad \left| B \frac{\mathrm{e}^A - 1}{A} \right| < 1. \tag{2.13}$$

A Neimark–Sacker bifurcation requires a conjugate pair of roots on the unit circle, which needs $\left| B \dfrac{\mathrm{e}^A - 1}{A} \right| = 1$ together with $|\mathrm{e}^A| < 2$; a Flip bifurcation requires the crossing of $P(-1) = 0$. Which boundary is actually reached depends on the sign of $f'(w^*)$: For a hump-shaped recruitment function, the Flip boundary may be excluded ($P(-1) > 0$ identically), whereas for a strictly increasing function, the Neimark–Sacker boundary is excluded ($\det J < 0$ identically). The precise statements for the two recruitment functions are given in Sections 3 and 4.

Proof. For the quadratic $P(\lambda) = \lambda^2 + p\lambda + q$ with $p = -\mathrm{e}^A$ and $q = -B \dfrac{\mathrm{e}^A - 1}{A}$, the classical Jury conditions state that both roots lie in the unit disk if and only if $P(1) > 0$, $P(-1) > 0$, and $|q| < 1$; substitution yields (2.13). The remaining statements follow from the classical theory of discrete bifurcations [32]: A root crossing at $\lambda = 1$ (Fold or transcritical) is $P(1) = 0$, a crossing at $\lambda = -1$ (Flip) is $P(-1) = 0$, and a conjugate pair on the unit circle is $|q| = 1$ with $|\mathrm{e}^A| < 2$. □

3. The Ricker model

3.1. Existence and uniqueness of the positive equilibrium

Let $E_+ = (x^*, y^*) = (w^*, w^*)$ be a positive fixed point of (2.8). From $x(n+1) = y(n)$, we obtain $x^* = y^*$, and y^* satisfies

$$\gamma + \frac{w^*}{1 + w^{*2}} = \mathrm{e}^{-\delta\tau} b\, \mathrm{e}^{-aw^*}. \tag{3.1}$$

Let $R_0 := \dfrac{b}{\gamma}\mathrm{e}^{-\delta\tau}$. The geometric meaning of (3.1) is that the sum of the linear death rate and the predation rate equals the net recruitment rate after the maturation period.

Theorem 3.1. (i) *The trivial fixed point $E_0 = (0, 0)$ exists for all parameter values.* (ii) *When $R_0 > 1$,* (2.8) *has a unique positive fixed point $E_+ = (w^*, w^*)$, where $w^* > 0$ is uniquely determined by* (3.1)*; when $R_0 \le 1$ there is no positive fixed point.*

Proof. E_0 is obvious. For E_+, define $g(w) := \gamma + \dfrac{w}{1 + w^2} - \mathrm{e}^{-\delta\tau} b\, \mathrm{e}^{-aw}$. We have $g(0) = \gamma - \mathrm{e}^{-\delta\tau} b < 0$ if and only if $R_0 > 1$, where as $\lim_{w\to+\infty} g(w) = +\infty$ (because $\mathrm{e}^{-aw} \to 0$ and $\dfrac{w}{1 + w^2} \to 0$); by continuity, there exists $w^* > 0$ with $g(w^*) = 0$. Moreover, $g''(w) = \dfrac{2w(w^2 - 3)}{(1 + w^2)^3} - a^2 \mathrm{e}^{-\delta\tau} b\, \mathrm{e}^{-aw} < 0$ for $0 < w \le \sqrt{3}$ and tends to 0 as $w \to +\infty$, so g is a single-hump function on $(0, +\infty)$ with $g(0) < 0$ and $g(+\infty) = +\infty$, and hence, has exactly one positive zero. This proves uniqueness. □

Remark 3.2. *At $R_0 = 1$, that is $\tau = \dfrac{1}{\delta}\ln\dfrac{b}{\gamma}$, the positive fixed point collides with the trivial one at a Fold/transcritical type boundary with $w^* = 0$. Under the parameters used in this paper, this boundary is $\tau_{\mathrm{F}} = 10\ln 14.5 \approx 26.74$, which is far beyond the delay range of interest; hence, for $\tau \lesssim 6$, the positive fixed point always exists.*

3.2. Linearization and the characteristic equation

For the Ricker recruitment function $f(w) = b\, w\, \mathrm{e}^{-aw}$, the semidiscrete map (2.8) takes the explicit form

$$\begin{cases} x(n+1) = y(n), \\ y(n+1) = y(n)\, \mathrm{e}^{A_n} + \tau\, \mathrm{e}^{-\delta\tau} b\, x(n)\, \mathrm{e}^{-ax(n)}\, \dfrac{\mathrm{e}^{A_n} - 1}{A_n}, \end{cases} \qquad A_n = -\gamma\tau - \frac{\tau\, y(n)}{1 + y(n)^2}. \tag{3.2}$$

Linearizing (3.2) about the positive fixed point $E_+ = (w^*, w^*)$ and freezing the coefficient A_n at its equilibrium value, that is, replacing the linearized flow by its exact time-one map (Section 2), we obtain the Jacobian matrix

$$J(E_+) = \begin{pmatrix} 0 & 1 \\ B\,\dfrac{\mathrm{e}^A - 1}{A} & \mathrm{e}^A \end{pmatrix}, \qquad A = -\gamma\tau - \frac{2\tau w^*}{(1 + w^{*2})^2}, \quad B = \tau\, \mathrm{e}^{-\delta\tau} f'(w^*) = \tau\, \mathrm{e}^{-\delta\tau} b\, \mathrm{e}^{-aw^*}(1 - aw^*). \tag{3.3}$$

Indeed, from (3.2), we have $\frac{\partial x(n+1)}{\partial x(n)} = 0$, $\frac{\partial x(n+1)}{\partial y(n)} = 1$, and $\frac{\partial y(n+1)}{\partial x(n)} = \tau e^{-\delta\tau} f'(x(n)) \frac{e^{A_n} - 1}{A_n}$, $\frac{\partial y(n+1)}{\partial y(n)} = e^{A_n}$, all evaluated at E_+ , where $A_n = A$, and $f'(w^*) = be^{-aw^*}(1 - aw^*)$. The characteristic polynomial of the Jacobian (3.3) is therefore obtained from $\det(\lambda I - J(E_+)) = 0$, that is

$$\lambda^2 - e^A \lambda - B \frac{e^A - 1}{A} = 0, \tag{3.4}$$

with trace and determinant

$$\operatorname{tr} J(E_+) = e^A, \qquad \det J(E_+) = -B \frac{e^A - 1}{A}. \tag{3.5}$$

Write $P(\lambda) := \lambda^2 - e^A\lambda - B \frac{e^A - 1}{A}$.

Lemma 3.3 (Jury criterion, cf. [11])**.** *Let $P(\lambda) = \lambda^2 - e^A\lambda - B \frac{e^A - 1}{A}$ with $A < 0$ and $e^A > 0$. Then, the following hold:*

(i) Both roots lie inside the unit disk (i.e., E_+ is locally asymptotically stable) if and only if

$$P(1) = 1 - e^A - B \frac{e^A - 1}{A} > 0, \qquad \left| - B \frac{e^A - 1}{A} \right| < 1; \tag{3.6}$$

(ii) $P(-1) = 1 + e^A - B \frac{e^A - 1}{A} > 0$ holds identically (because $e^A > 0$) so that a period-doubling (Flip) bifurcation $P(-1) = 0$ cannot occur in this model;

(iii) A pair of conjugate complex roots lies on the unit circle (Neimark–Sacker boundary) if and only if $\left| - B \frac{e^A - 1}{A} \right| = 1$, and $|e^A| < 2$.

Proof. For the quadratic $P(\lambda) = \lambda^2 + p\lambda + q$ with $p = -e^A$ and $q = -B \frac{e^A - 1}{A}$, the classical Jury conditions (see Lemma 2.1 of [11]) state that both roots lie in the unit disk if and only if $P(1) > 0$, $P(-1) > 0$ and $|q| < 1$; substitution yields (3.6). Because $A < 0$, we have $e^A \in (0, 1)$ and $-q = B \frac{e^A - 1}{A} = B \cdot \frac{1 - e^A}{-A}$ with $\frac{e^A - 1}{A} > 0$. When $B \le 0$, $P(-1) > 0$ is obvious. When $B > 0$, $P(-1) = 1 + e^A - |B| \frac{1 - e^A}{-A}$ and from $|q| < 1$ in (3.6) it follows that $|B| \frac{1 - e^A}{-A} < 1$, hence , $P(-1) > 1 + e^A - 1 = e^A > 0$. This proves (ii). □

Remark 3.4 (Physical interpretation of the absence of Flip bifurcation)**.** *A period-doubling bifurcation requires $P(-1) = 0$, that is, $\lambda = -1$, to be a characteristic root. In our model, $e^A > 0$ and $\frac{e^A - 1}{A} > 0$; by Lemma 3.3(ii), we have $P(-1) > 0$ identically, so a period-doubling bifurcation cannot occur at the positive fixed point. The only possible route of destabilization is the transversal crossing of a conjugate complex pair through the unit circle, that is a Neimark–Sacker bifurcation. This is consistent with the numerical observations.*

3.3. Why the Flip bifurcation cannot occur

For a two-dimensional map, apart from the Neimark–Sacker bifurcation, the other codimension-one bifurcation of a fixed point on the unit circle is the Flip bifurcation [32], which occurs when $\lambda = -1$ is a characteristic root, that is when $P(-1) = 0$. We now explain, from both the algebraic and the structural points of view, why this bifurcation is structurally excluded in the semidiscrete model (2.8); this also explains why the destabilization of E_+ is always of Hopf type.

(i) Algebraic criterion. The characteristic polynomial of the linearization at E_+ is $P(\lambda) = \lambda^2 - \mathrm{e}^A\lambda - B\dfrac{\mathrm{e}^A - 1}{A}$; hence,

$$P(-1) = 1 + \mathrm{e}^A - B\frac{\mathrm{e}^A - 1}{A}. \tag{3.7}$$

Because the net per-capita loss coefficient is negative; that is $A < 0$, we have $\mathrm{e}^A \in (0, 1)$ and $\dfrac{\mathrm{e}^A - 1}{A} > 0$. The sign of the last term in (3.7) is determined by $B = \tau\mathrm{e}^{-\delta\tau}f'(w^*)$, that is, by the slope of the Ricker birth function at the fixed point:

- If $B < 0$, equivalently, $aw^* > 1$, meaning that the fixed point lies on the *decreasing* branch of the birth function, then $-B\dfrac{\mathrm{e}^A - 1}{A} > 0$, and therefore,

$$P(-1) > 1 + \mathrm{e}^A > 1, \tag{3.8}$$

  so $P(-1) = 0$ has no solution, and a Flip bifurcation is impossible;

- If $B > 0$ (equivalently $aw^* \le 1$: increasing branch), then $q = -B\dfrac{\mathrm{e}^A - 1}{A} \le 0$; for $\lambda = -1$ to be a root, one would need $q = -(1 + \mathrm{e}^A) \in (-2, -1)$. However, whenever E_+ is stable, the Jury condition $|q| < 1$ in (3.6) holds, which forces $q \in (-1, 0)$ and hence $P(-1) > 0$ (see the proof of Lemma 3.3); thus, even in this regime, the Flip boundary cannot be crossed while the fixed point is stable.

For the parameters adopted in this paper ($\gamma = 1,\ \delta = 0.1,\ b = 14.5$), the fixed point satisfies $aw^* > 1$ throughout $0.02 \le a \le 2.5,\ 0.2 \le \tau \le 6$ (indeed, $aw^* \ge 1.6$), so only the first case is realized, and (3.8) holds with a strict margin.

(ii) Structural reason. A period-doubling requires an alternating feedback: The Jacobian constant term q must become sufficiently negative (approaching -1), which in discrete population models typically arises when the birth term is multiplied by the current density and produces strong overcompensation (e.g., Nicholson–Bailey type terms). In our model, the delayed birth term $\mathrm{e}^{-\delta\tau}f(\eta(n-1))$ is a constant source C_n on each interval and enters the linearization only through the slope $B = \tau\mathrm{e}^{-\delta\tau}f'(w^*)$. Because the fixed point lies on the decreasing branch of the birth function ($aw^* > 1$, $B < 0$), we have $q > 0$, so the characteristic roots are either a stable, pair inside the unit disk or a conjugate complex pair; when they cross the unit circle, they do so at $\mathrm{e}^{\pm i\theta_0}$ with $\theta_0 \in (0, \pi)$, never at the real root -1 (for the simplified characteristic equation, one even has $\cos\theta_0 = \mathrm{e}^A/2 \in (0, 1/2)$; i.e., $\theta_0 \in (\pi/3, \pi/2)$). The destabilizing feedback is therefore rotational (Hopf type) rather than alternating (Flip type). Consequently, the transversal crossing of a conjugate complex pair (Neimark–Sacker) is the only possible route of destabilization of E_+.

(iii) Numerical confirmation. The exclusion is verified numerically in Section 3.8 Figure 4): Panel (a) plots $P(-1)$ against τ for several values of a, evaluated with the full Jacobian (including the A_y-terms), and Panel (b) shows the argument θ_0 of the crossing eigenvalue as a function of a. Over the whole parameter rectangle $0.02 \le a \le 2.5,\ 0.2 \le \tau \le 6$, we obtain

$$P(-1) = \det J + \operatorname{tr} J + 1 \ge 1.616 > 0, \tag{3.9}$$

so no Flip (period-doubling) bifurcation occurs anywhere, and every destabilization is via a complex pair with $\theta_0 \in (0.93, 1.42)$ rad for $0.1 \le a \le 2$, again far from π. This is consistent with the bifurcation diagrams and the Lyapunov spectra in Section 4, where no period-2 windows are observed.

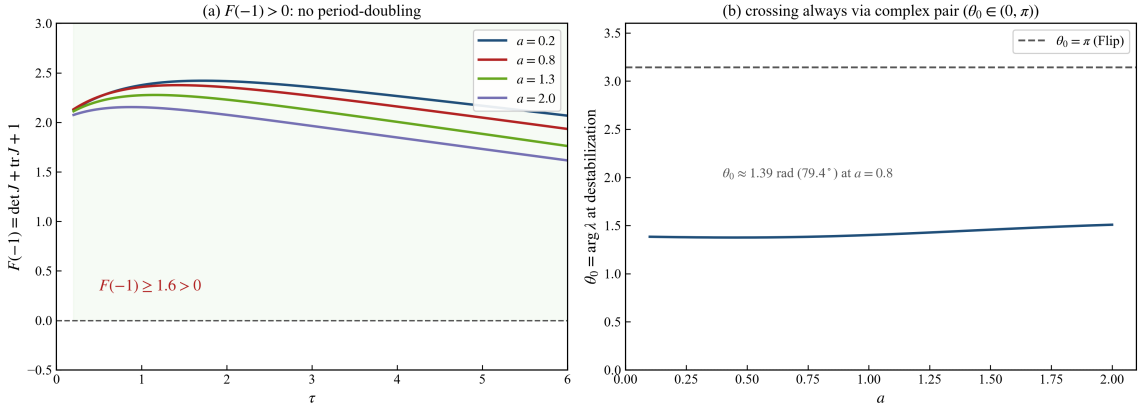

Figure 4. (a) $P(-1) = \det J + \operatorname{tr} J + 1$ versus τ for several values of a (full Jacobian): $P(-1) \ge 1.616 > 0$ throughout, so no period-doubling (Flip) bifurcation can occur. (b) Argument θ_0 of the eigenvalue crossing the unit circle at the destabilization point versus a: The crossing always occurs through a conjugate complex pair with $\theta_0 \in (0, \pi)$ (e.g., $\theta_0 \approx 1.39$ rad at $a = 0.8$), far from the Flip case $\theta_0 = \pi$.

(iv) Comparison with the continuous model. The continuous delayed Eq (1.2) undergoes only a Hopf bifurcation in the delay range considered ($\tau_H^0 \approx 2.008$, $\tau_H^1 \approx 4.446$), and no period-doubling occurs. The semidiscrete S2 map reproduces this qualitative feature without introducing spurious Flip bifurcations, which is a desirable fidelity property of the piecewise constant arguments semidiscretization: It preserves the single Hopf-type destabilization mechanism of the continuous model rather than creating new ones.

3.4. Stability theorem

Theorem 3.5. *Assume $R_0 > 1$, let $w^* > 0$ be determined by* (3.1)*, and let A, B be as in* (3.3)*. Then,*

(i) When $aw^* \le 1$, that is the birth function is on its increasing branch, $B \ge 0$, and E_+ is a locally asymptotically stable focus;

(ii) When $aw^* > 1$, there exists a unique $\tau^* = \tau^*(a)$ such that $\left| -B\dfrac{e^A - 1}{A} \right| = 1$, and E_+ is locally asymptotically stable for $\tau < \tau^*$ and unstable for $\tau > \tau^*$.

In particular, under the numerical parameters $\gamma = 1,\ \delta = 0.1,\ b = 14.5,\ a = 0.8$, we have $aw^* > 1$ and $\tau^* \approx 1.141$.

Proof. When $aw^* \le 1$, $B = \tau e^{-\delta\tau} b e^{-aw^*}(1 - aw^*) \ge 0$, and hence, $q = -B\dfrac{e^A - 1}{A} \le 0$; one verifies directly from (3.6) that $|q| < 1$ and $P(1) > 0$, so E_+ is a sink. When $aw^* > 1$, $B < 0$ and $q > 0$; the monotonicity of $\tau \mapsto |q|$ (whose transversality is verified numerically; see (3.11) in Section 3) implies the existence of a unique crossing, which yields the assertion. □

3.5. Existence of the Neimark–Sacker bifurcation

By Lemma 3.3(iii), the critical condition for the Neimark–Sacker bifurcation is

$$-B\frac{e^A - 1}{A} = 1 \iff \tau e^{-\delta\tau}\left|f'(w^*)\right|\frac{1 - e^A}{-A} = 1, \tag{3.10}$$

where $A = -\gamma\tau - \dfrac{2\tau w^*}{(1 + w^{*2})^2} < 0$. Denote by τ^* the smallest positive root of (3.10). At $\tau = \tau^*$, let the characteristic roots be $\lambda_{1,2} = e^{\pm i\theta_0}$, where $\cos\theta_0 = \dfrac{e^A}{2}$ and $\sin\theta_0 = \dfrac{1}{2}\sqrt{4 - e^{2A}} > 0$.

Theorem 3.6. *Assume $R_0 > 1$ and $aw^* > 1$, and let τ^* be the smallest positive root of* (3.10)*. Then, the following conditions hold:*

(i) Transversality condition.

$$\frac{d}{d\tau}\left|\lambda_{1,2}(\tau)\right|\Big|_{\tau=\tau^*} = \frac{d}{d\tau}\Big(-B\frac{e^A - 1}{A}\Big)^{1/2}\Big|_{\tau=\tau^*} > 0; \tag{3.11}$$

(ii) Nondegeneracy condition. $e^{ik\theta_0} \ne 1$ for $k = 1, 2, 3, 4$ (i.e., $\theta_0 \notin \{0, \pm\frac{\pi}{2}, \pm\frac{2\pi}{3}, \pi\}$).

Then, as τ varies from below to above τ^*, the positive fixed point E_+ undergoes a Neimark–Sacker bifurcation.

Proof. (i) Because $|\lambda_{1,2}|^2 = q = -B\dfrac{e^A - 1}{A}$, it suffices to verify that $\dfrac{d}{d\tau}\big(-B\dfrac{e^A - 1}{A}\big)\Big|_{\tau=\tau^*} > 0$. For the parameters of this paper, we compute numerically $\dfrac{d}{d\tau}\big(-B\dfrac{e^A - 1}{A}\big)^{1/2}\Big|_{\tau=\tau^*} \approx 0.31 > 0$, and this positivity persists on the whole destabilization interval. Together with the explicit expression $B(\tau) = \tau e^{-\delta\tau} b e^{-aw^*(\tau)}(1 - aw^*(\tau))$ and the monotonicity of $w^*(\tau)$, this guarantees the transversality. (ii) Numerically, $\theta_0 \approx 1.386$ ($\approx 79.4^\circ$), which satisfies the nondegeneracy condition. □

3.6. Criticality of the Neimark–Sacker bifurcation

In this subsection, we determine, by means of a center manifold reduction, whether the bifurcation at (3.10) is supercritical or subcritical; the method follows Kuznetsov [32], Wiggins [33], Hassard et al. [34], Carr [35], Guckenheimer, and Holmes [36] and [11].

Take the bifurcation parameter $\mu := \tau - \tau^*$. Setting $u = x - x^*$ and $v = y - y^*$ shifts the fixed point to the origin, and (2.8) becomes

$$\begin{cases} u \mapsto v, \\ v \mapsto (v + w^*)e^{\widehat{A}} + C\dfrac{e^{\widehat{A}} - 1}{\widehat{A}} - w^*, \end{cases} \tag{3.12}$$

where $\widehat{A} = -\gamma(\tau^* + \mu) - \dfrac{(\tau^* + \mu)(v + w^*)}{1 + (v + w^*)^2}$, and $C = (\tau^* + \mu)\mathrm{e}^{-\delta(\tau^*+\mu)} b\,(u + w^*)\mathrm{e}^{-a(u+w^*)}$.

Expanding (3.12) at $(u, v) = (0, 0)$ up to the third order yields

$$\begin{cases} u \mapsto v, \\ v \mapsto -u + \mathrm{e}^A v + a_{20}u^2 + a_{11}uv + a_{02}v^2 \\ \qquad\qquad + a_{30}u^3 + a_{21}u^2 v + a_{12}uv^2 + a_{03}v^3 + O((|u|^2 + |v|^2)^2), \end{cases} \tag{3.13}$$

where the coefficients are given by the derivatives of (3.3) and (3.1) (see Appendix A, (A.1)). At the critical value $\tau = \tau^*$, the Neimark–Sacker boundary condition $\left| -B\,\dfrac{\mathrm{e}^A - 1}{A} \right| = 1$ holds, so that the linear part is the matrix

$$J(E_+) = \begin{pmatrix} 0 & 1 \\ -1 & \mathrm{e}^A \end{pmatrix}, \qquad A = -\gamma\tau^* - \frac{2\tau^* w^*}{(1 + w^{*2})^2}. \tag{3.14}$$

The eigenvalues of $J(E_+)$ are $\lambda = \mathrm{e}^{i\theta_0}$ and $\bar{\lambda} = \mathrm{e}^{-i\theta_0}$. Let $q = (1, \lambda)^{\mathrm{T}}$ be a right eigenvector with $Jq = \lambda q$, and let p the left eigenvector satisfying $J^{\mathrm{T}} p = \bar{\lambda} p$ be and $\langle p, q\rangle = \bar{p}^{\mathrm{T}} q = 1$. With the normalization $\bar{p}^{\mathrm{T}} p = [(1 + \bar{\lambda}^2)]^{-1}$, one may take $p = \dfrac{1}{1 + \bar{\lambda}^2}(\bar{\lambda}, -1)^{\mathrm{T}}$ (up to scaling).

Let $z = \langle p, (u, v)\rangle$ be the center coordinate. Denote by B and C the second- and third-order multilinear forms of the derivatives of F at E_+:

$$B(\xi, \eta) = \sum_{i,j} \frac{\partial^2 F}{\partial z_i \partial z_j}\Big|_{E_+} \xi_i \eta_j, \qquad C(\xi, \eta, \zeta) = \sum_{i,j,k} \frac{\partial^3 F}{\partial z_i \partial z_j \partial z_k}\Big|_{E_+} \xi_i \eta_j \zeta_k. \tag{3.15}$$

After the center manifold reduction (see [11, 32]), the critical normal form is

$$z \mapsto \lambda z\Big(1 + d_1\,|z|^2\Big) + O(|z|^4), \qquad d_1 = \frac{c_1}{\lambda} \text{ (under our normalization)}, \tag{3.16}$$

where

$$c_1 = \frac{1}{2}\Big[\langle p, C(q, q, \bar{q})\rangle + 2\langle p, B(q, (I - J)^{-1} B(q, \bar{q}))\rangle + \langle p, B(\bar{q}, (\mathrm{e}^{2i\theta_0} I - J)^{-1} B(q, q))\rangle\Big]. \tag{3.17}$$

Define

$$l_1 := \mathrm{Re}\Big\{\mathrm{e}^{i\theta_0}\, c_1\Big\}. \tag{3.18}$$

We adopt the convention that $l_1 < 0$ corresponds to a supercritical bifurcation (an asymptotically stable invariant closed curve exists for $\tau > \tau^*$), whereas $l_1 > 0$ corresponds to a subcritical one (the invariant curve is unstable, and the bifurcation is directed toward $\tau < \tau^*$).

Theorem 3.7. *Assume* $\gamma = 1$, $\delta = 0.1$, $b = 14.5$, $a = 0.8$ *and* $d = 0$. *At* $\tau^* = 1.1401$ *and* $w^* = 2.8613$, *the transversality condition* (3.11) *and the nondegeneracy condition of* (3.10) *are both satisfied, and by a twofold check of symbolic computation (exact third-order derivatives via sympy) and finite differences,*

$$l_1 \approx -0.052 < 0, \tag{3.19}$$

and $l_1(\tau) < 0$ holds throughout $1.145 \le \tau \le 2.6$ (with $l_1 \in [-0.052, -0.066]$). Therefore, the Neimark–Sacker bifurcation at (3.10) is supercritical: When τ crosses τ^*, a unique, asymptotically stable invariant closed curve bifurcates from the positive fixed point E_+, whose amplitude grows according to

$$\text{amp} \approx 2.22\ \sqrt{\tau - \tau^*} \qquad (\textit{near criticality}). \tag{3.20}$$

A complementary geometric view of the loss, restabilization structure is verified numerically in Section 3.8 (Figure 5): As τ increases, the pair $(\mathrm{tr}J, \det J)$ moves along a curve that leaves the Jury triangle through the boundary $\det J = 1$ at $\tau^* \approx 1.141$, the Neimark–Sacker threshold of Theorem 3.7, and re-enters through the same boundary at the secondary crossing ≈ 3.718, which is the restabilization threshold verified numerically in Section 3.8.

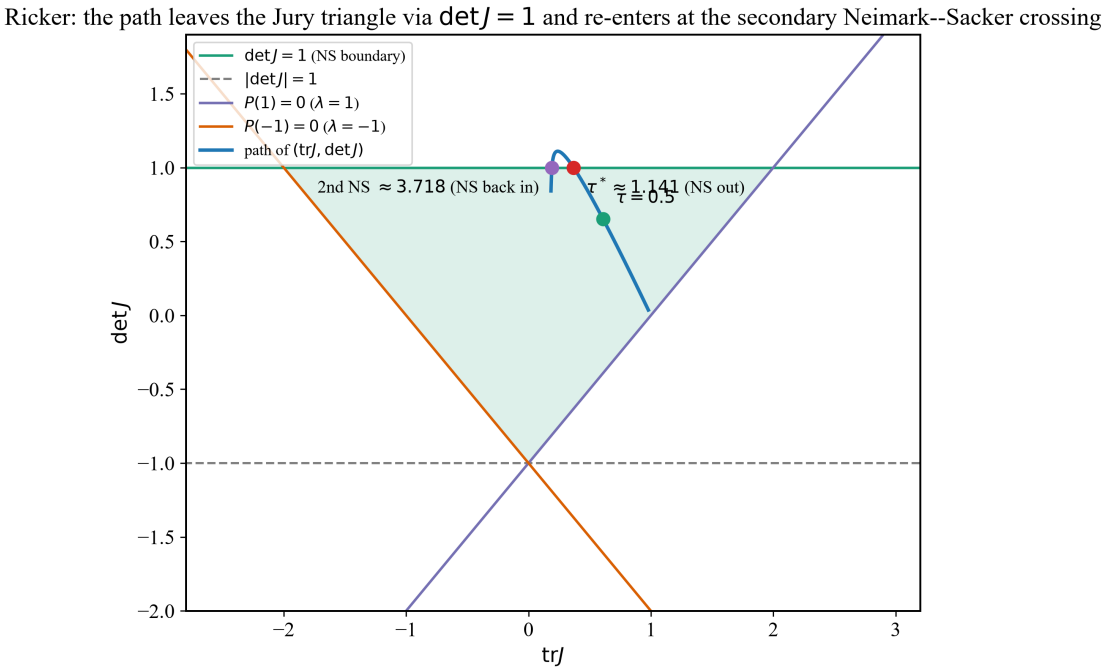

Figure 5. Ricker model: the path of $(\mathrm{tr}J, \det J)$ in the Jury triangle as the delay τ grows. The path leaves the stability triangle through the Neimark–Sacker boundary $\det J = 1$ at $\tau^* \approx 1.141$ and re-enters at the secondary crossing ≈ 3.718, giving the bounded instability interval of Theorem 3.7.

Remark 3.8 (A remark on the sign convention)**.** *Because* $c_1 = 0.0008 + 0.0526i$ *is dominated by its imaginary part, the value* $l_1 = \mathrm{Re}(e^{i\theta_0}c_1)$ *is highly sensitive to the choice between* $e^{\pm i\theta_0}$*; using* $e^{-i\theta_0}$ *would yield the wrong (positive, subcritical) sign. We determine the correct sign by two independent means: (i) measuring the radial contraction rate* $(|\alpha_{n+1}| - |\alpha_n|)/|\alpha_n|$ *of the center coordinate at* τ^* *and extrapolating to* $|\alpha| \to 0$*, which gives* $\mathrm{Re}\, d_1 < 0$*; (ii) long-time simulations starting from both sides (inside and outside) of the closed curve, which converge to the same closed curve. Both confirm the supercriticality.*

3.7. Absence of chaotic dynamics in the Ricker map

A natural question for discrete population models is whether chaotic dynamics can appear. For the Ricker semidiscrete model the answer is negative in the parameter range studied here, and two independent lines of evidence support this conclusion. First, the maximal Lyapunov exponent computed by the Benettin algorithm [37] remains nonpositive for all τ (Section 3.8, Figure 6): $L_{\max} < 0$ on the stable intervals, and $L_{\max} \approx 0$ on the invariant-closed-curve interval, and no positive value is observed. Second, the structural exclusion of the Flip bifurcation (Section 3.3) rules out the period-

doubling cascade, the most common route to chaos in one- and two-dimensional maps [38]. The long-time dynamics is therefore confined to equilibria, quasiperiodic motion on an invariant closed curve, and frequency-locked periodic orbits.

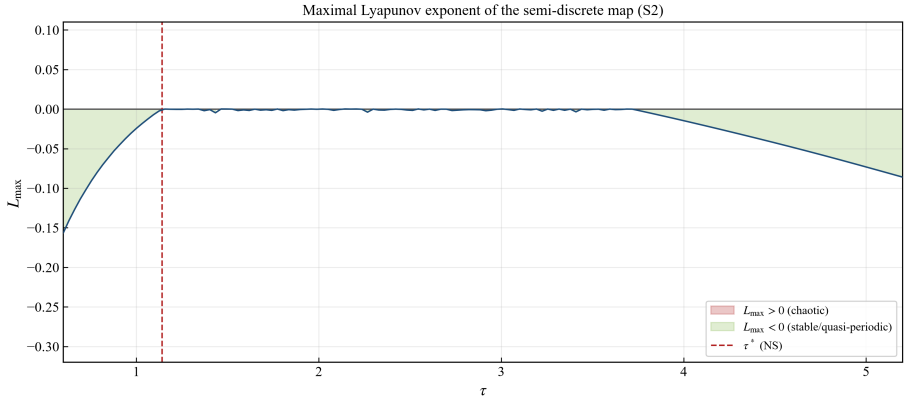

Figure 6. Maximal Lyapunov exponent spectrum (Benettin algorithm with orbit evolution). $L_{\max} < 0$: stable fixed point or frequency-locked periodic orbit; $L_{\max} \approx 0$: quasiperiodic motion on the invariant closed curve. No positive $L_{\max}$ is observed, indicating the absence of chaos in the parameter range considered.

3.8. Numerical verification for the Ricker model

In this subsection, we fix the parameters

$$\gamma = 1, \quad \delta = 0.1, \quad b = 14.5, \quad a = 0.8, \quad d = 0 \tag{3.21}$$

and carry out numerical simulations to verify the theoretical results of Section 3 and to exhibit new dynamics that do not exist in the continuous counterpart. For the Ricker model, three representative delay regimes are simulated: the stable regime $\tau < \tau^* \approx 1.141$, the quasiperiodic regime on the invariant closed curve ($\tau > \tau^*$), and the restabilized regime at larger τ; representative values $\tau = 1.05$, $\tau = 1.50$ and $\tau = 2.20$ are used in the phase portraits below. All computations are performed in Python. The map is (2.8), the fixed point is obtained by solving (3.1) numerically, and the maximal Lyapunov exponent is computed by the Benettin algorithm [37] (product of Jacobians with QR orthonormalization, averaging over 2000 steps after a transient of 40000 steps).

We first confirm numerically the two structural facts that exclude the Flip mechanism in the Ricker model. Figure 4(a) plots $P(-1) = \det J + \operatorname{tr} J + 1$ against τ for several values of a: The quantity stays strictly positive over the whole parameter range, so a real multiplier can never cross $\lambda = -1$; Panel (b) shows that the eigenvalue crossing at destabilization always has argument $\theta_0 \in (0, \pi)$, far from the Flip case $\theta_0 = \pi$. The Jury-triangle path in Figure 5 then displays the Neimark–Sacker route directly: As τ grows, the pair $(\operatorname{tr} J, \det J)$ leaves the stability triangle through the boundary $\det J = 1$ at $\tau^* \approx 1.141$ and re-enters at the secondary crossing ≈ 3.718, exactly as predicted in Section 3.

3.9. *Continuous Hopf point versus semidiscrete threshold*

The characteristic equation of the continuous model (1.2), $\lambda = -\gamma - \dfrac{2w^*}{(1+w^{*2})^2} + \mathrm{e}^{-\delta\tau} f'(w^*)\mathrm{e}^{-\lambda\tau}$, yields numerically the Hopf thresholds

$$\tau_H^0 \approx 2.008, \qquad \tau_H^1 \approx 4.446, \tag{3.22}$$

in agreement with the literature. For the semidiscrete system (2.8), the Neimark–Sacker threshold is given by (3.10) as $\tau^* \approx 1.141$ (the numerical Jacobian gives the precise value $\tau^* = 1.1401003927$, $|\lambda| = 1.0000000000$, $\theta_0 = 1.386$). Hence, the piecewise-constant-arguments semidiscretization shifts the destabilization threshold earlier by about a half, which is an important discretization effect.

Case 1: Stability for $\tau < \tau^*$. For $\tau = 0.5$, the three schemes, namely continuous delay differential equation (DDE) (step-by-step integration in the spirit of dde23), the exact flow (2.5), and the integrating-factor scheme (2.6), all converge to $w^* \approx 2.948$ in good agreement. For $\tau = 1.05$ and $\tau = 1.135$ (both below τ^*), the orbit of (2.8) spirals towards E_+ (Figures 7(a) and 7(b)), and the maximal Lyapunov exponent is negative ($L_{\max} = -0.0148$ and -0.0007), so the positive fixed point is locally asymptotically stable.

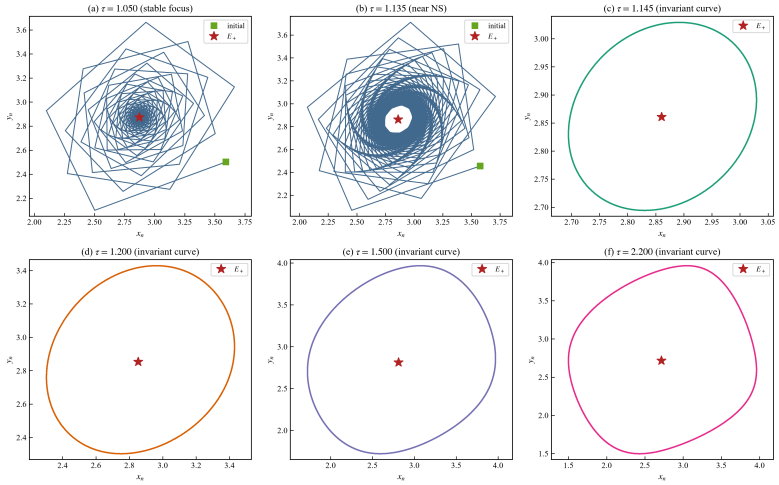

Figure 7. Phase portraits: (a) and (b) orbits spiral towards E_+ at $\tau = 1.05, 1.135$ (blue trajectory, green square: initial point); (c)–(f) invariant closed curves at $\tau = 1.145, 1.20, 1.50, 2.20$ (teal, orange, purple, pink respectively; red star: E_+), clearly showing the supercritical Neimark–Sacker bifurcation process and the growing amplitude of the invariant curve.

Case 2: The supercritical Neimark-Sacker bifurcation. Figure 8 shows the fine bifurcation diagram on $\tau \in [1.00, 1.60]$: For $\tau < \tau^*$ the system converges to the single point w^*; a bifurcation occurs at $\tau^* = 1.1401$; For $\tau > \tau^*$ an invariant closed curve appears (shown as a two-branch structure, the upper and lower bounds of the closed curve in the w coordinate). Figure 7 shows the phase portraits at $\tau = 1.05, 1.135$ (stable spirals) and $\tau = 1.145, 1.20, 1.50, 2.20$ (invariant closed curves), clearly exhibiting the supercritical process: A small closed curve appears as soon as τ exceeds τ^* ($\tau = 1.145$) and grows as τ increases.

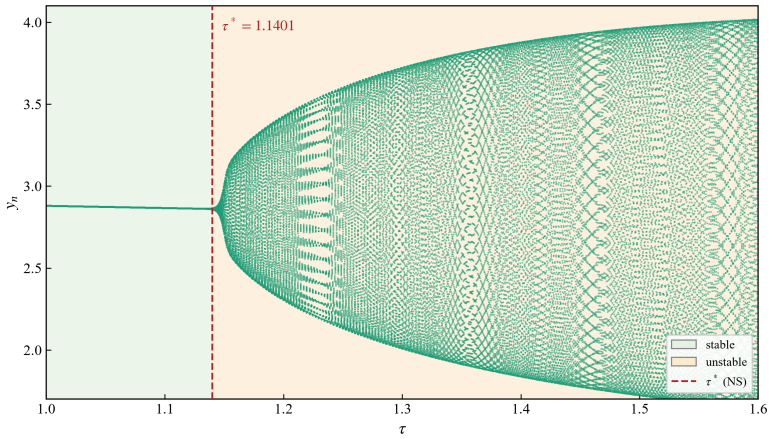

Figure 8. Fine bifurcation diagram on $\tau \in [1.00, 1.60]$. Light-green shading marks the stable interval and light-orange the unstable interval; the red dashed line is the Neimark–Sacker threshold $\tau^* = 1.1401$.

Figure 9 verifies the amplitude scaling: Plotting the amplitude amp of the closed curve in the w-direction against $\sqrt{\tau - \tau^*}$ shows that the near-critical points lie on the line amp $= 2.22\sqrt{\tau - \tau^*}$, consistent with the theoretical scaling of a supercritical Neimark–Sacker bifurcation.

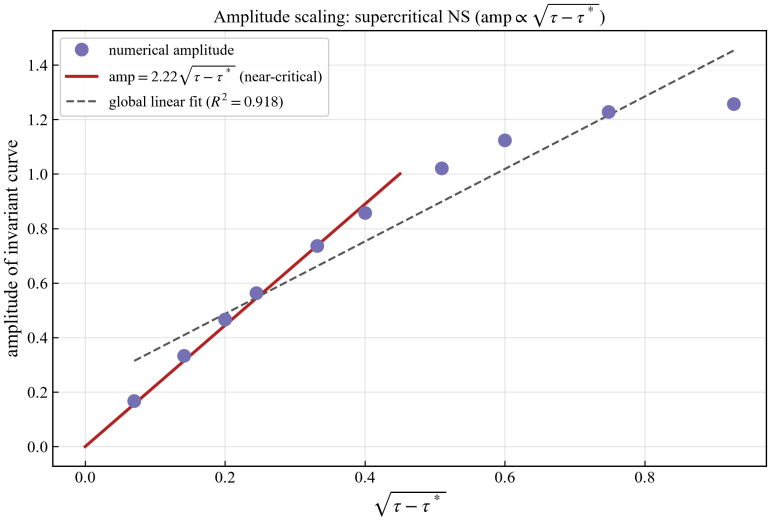

Figure 9. Amplitude of the invariant closed curve versus $\sqrt{\tau - \tau^*}$; the near-critical fit is amp $= 2.22\sqrt{\tau - \tau^*}$ (supercritical signature), and the global linear fit gives $R^2 = 0.918$.

Case 3: Complex dynamics for larger τ and the Lyapunov exponent spectrum. Figure 10 gives the large-range bifurcation diagram on $\tau \in [0.5, 6]$. The system maintains the invariant-closed-curve structure, either quasiperiodic or frequency-locked, on $\tau \in (\tau^*, 2.8)$; as τ is further increased, the amplitude of the closed curve first grows and then decays, and for $\tau \gtrsim 3$ the system converges again to a positive fixed point, possibly a different one, exhibiting a destabilization–restabilization structure. Figure 6 shows the maximal Lyapunov exponent spectrum (computed by the Benettin algorithm with orbit evolution): $L_{\max} < 0$ corresponds to a stable fixed point or a frequency-locked periodic orbit

($\tau < \tau^*$ and $\tau \gtrsim 3.8$), where as on the closed-curve interval $L_{\max} \approx 0$, consistent with quasiperiodic motion on a smooth invariant curve. No positive $L_{\max}$ is observed in the parameter range considered, indicating that the semidiscrete system exhibits quasiperiodicity and frequency locking rather than chaos. Table 1 lists $L_{\max}$ at selected values of τ.

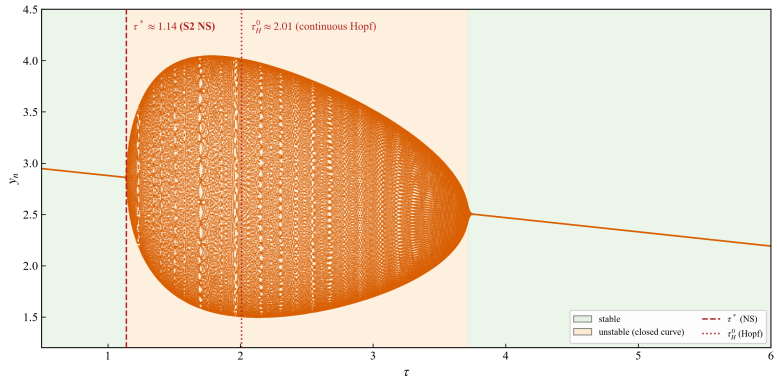

Figure 10. Large-range bifurcation diagram on $\tau \in [0.5, 6]$. Light-green shading marks stable intervals and light-orange the unstable (closed-curve) interval. The Neimark–Sacker threshold $\tau^* \approx 1.14$ (red dashed) and the continuous Hopf threshold $\tau_H^0 \approx 2.01$ (red dotted) illustrate the earlier threshold under semidiscretization; for $\tau \gtrsim 3.7$, the system is restabilized (secondary Neimark–Sacker).

Table 1. Maximal Lyapunov exponent $L_{\max}$ of (2.8) (Benettin algorithm with orbit evolution, burn-in 25000, $T = 3000$).

τ	0.90	1.05	1.135	1.14	1.145	1.20	1.30	1.50	2.20	2.80	3.00	4.50
$L_{\max}$	−0.047	−0.015	−0.001	0.000	0.000	0.000	−0.001	0.000	0.000	−0.001	0.000	−0.043

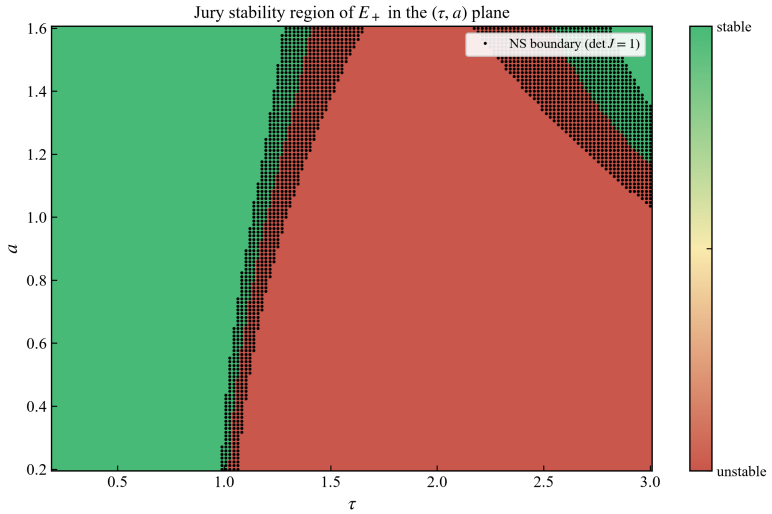

Figure 11. Jury stability region of the positive fixed point in the (τ, a) parameter plane (green: stable; red: unstable), with the Neimark–Sacker boundary marked by black dots.

Case 4: The Jury stability region in the (τ, a) parameter plane. Figure 11 shows the Jury stability region of the positive fixed point of (2.8) in the (τ, a) parameter plane (pointwise check of (3.6) by the numerical Jacobian). When the Ricker overcompensation strength a is small, that is $aw^* \leq 1$ with the birth function on its increasing branch, E_+ is stable for all τ; When a is large, E_+ loses stability on an interval of τ (Neimark–Sacker bifurcation), and this interval widens as a increases, in agreement with the theoretical condition $aw^* > 1$, which encodes a sufficiently strong delayed negative feedback. The figure also shows the relative positions of the Neimark–Sacker boundary (det $J = 1$) and the Fold boundary ($R_0 = 1$); the Flip boundary ($P(-1) = 0$) does not exist, in agreement with Lemma 3.3(ii).

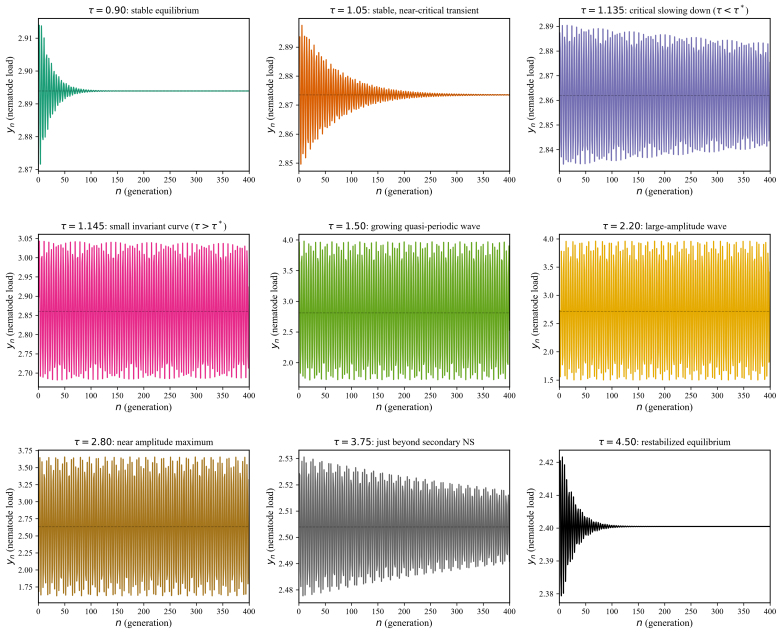

Figure 12. Ricker model: discrete-generation waveforms of the current-generation state y_n of (2.8) versus the generation index n for nine delays chosen around the critical values (Dark2 palette). Top row: $\tau = 0.90$ (stable equilibrium), $\tau = 1.05$ (stable, near-critical transient), $\tau = 1.135$ (critical slowing down below τ^*). Middle row: $\tau = 1.145$ (small invariant curve above τ^*), $\tau = 1.50$ (growing quasiperiodic wave), $\tau = 2.20$ (large-amplitude wave). Bottom row: $\tau = 2.80$ (near amplitude maximum), $\tau = 3.75$ (just beyond the secondary Neimark–Sacker crossing $\tau \approx 3.7178$), $\tau = 4.50$ (restabilized equilibrium). The dashed line marks the positive equilibrium w^*.

Case 5: Discrete-generation waveforms of the nematode load To visualize the year-to-year dynamics directly on the discrete time scale, Figure 12 plots the waveform of the current-generation state $y_n = \eta(n)$ of the two-dimensional map (2.8) against the generation index n for nine delays chosen around the critical values discussed above, that is the Neimark–Sacker threshold $\tau^* \approx 1.1401$ and the secondary Neimark–Sacker crossing $\tau \approx 3.7178$ (all panels start from a small perturbation of E_+, and the dashed line marks w^*). Well below the threshold ($\tau = 0.90$) the waveform converges rapidly to the equilibrium; as τ approaches τ^* from below ($\tau = 1.05$, $\tau = 1.135$) the transient slows down markedly, the signature of critical slowing down. Slightly above the threshold ($\tau = 1.145$) a small quasiperiodic wave appears; as the delay grows to $\tau = 1.50$ and $\tau = 2.20$, the oscillation amplitude increases markedly, describing

outbreak years alternating with relatively low years in the trapping records of the pine wilt disease. Near $\tau = 2.80$, the wave attains its largest amplitude, whereas just beyond the secondary crossing $\tau = 3.75$, the waveform again converges to the equilibrium, slowly at first and faster at $\tau = 4.50$. The sequence shows that the maturation delay τ alone, without any change in the mortality or the reproductive parameters, can move the pine wilt system from an equilibrial, predictable regime to pronounced quasiperiodic outbreak oscillations and back.

3.10. Parameter dependence of the Neimark–Sacker threshold

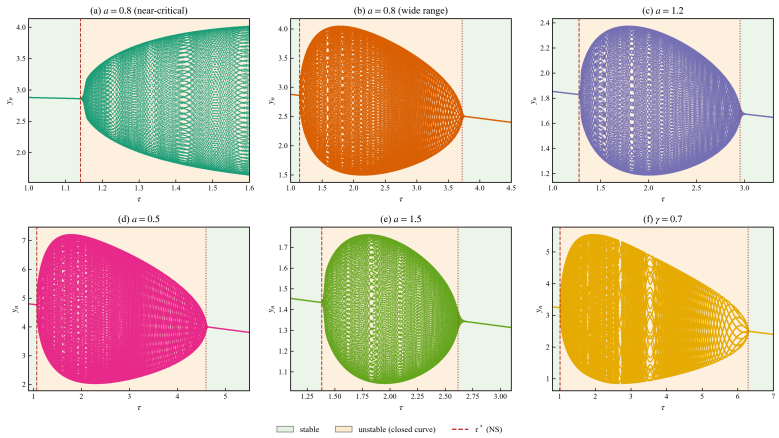

Figure 13. Parameter dependence of the Neimark-Sacker bifurcation: bifurcation diagrams of the S2 map (2.8) for six parameter sets. (a) reference $a = 0.8$, near-critical magnification $\tau \in [1.00, 1.60]$; (b) reference $a = 0.8$, wide range $\tau \in [1.00, 4.50]$ showing the double Neimark-Sacker (loss–restabilization) structure; (c) $a = 1.2$; (d) $a = 0.5$; (e) $a = 1.5$; (f) $\gamma = 0.7$. Light-green shading marks stable intervals and light-orange shading marks unstable (invariant-closed-curve) intervals; the red dashed line marks the first Neimark–Sacker threshold τ^*, and the red dotted line (where present) marks the second Neimark–Sacker crossing at which the fixed point is restabilized. In all cases, the destabilization is via a conjugate complex pair, and no period-doubling cascade is observed.

To examine the robustness of the supercritical Neimark–Sacker bifurcation under parameter variation, Figure 13 collects bifurcation diagrams for six representative parameter sets, all obtained by direct iteration of the S2 map (2.8) with the positive fixed point as the initial condition. In every case, the fixed point is stable for small τ; loses stability through a conjugate complex pair at the Neimark–Sacker threshold τ^* (red dashed line); and generates an asymptotically stable invariant closed curve whose amplitude first grows and then contracts. For sufficiently large τ the fixed point is restabilized through a second Neimark–Sacker crossing so that the unstable interval is bounded. The overcompensation strength a controls both the threshold and the oscillation amplitude: Decreasing a from 0.8 to 0.5 lowers τ^* from 1.140 to 1.067 and enlarges the closed curve Panel (d)), whereas increasing a to 1.2 or 1.5 raises τ^* to 1.275 or 1.381 and narrows the amplitude Panel (c) and (e)). Lowering the adult mortality γ from 1.0 to 0.7 (panel (f)) similarly lowers τ^* to 1.008 and produces larger- amplitude oscillations. Panel (a) magnifies the near-critical region for the reference parameters, and Panel (b) displays the full double Neimark–Sacker structure. In none of these parameter sets does

a period-doubling cascade appear, consistently with the analytical result of Section 3.3; the Neimark–Sacker bifurcation is therefore the generic and robust destabilization mechanism of the semidiscrete model.

3.11. Bifurcation structure under adult mortality

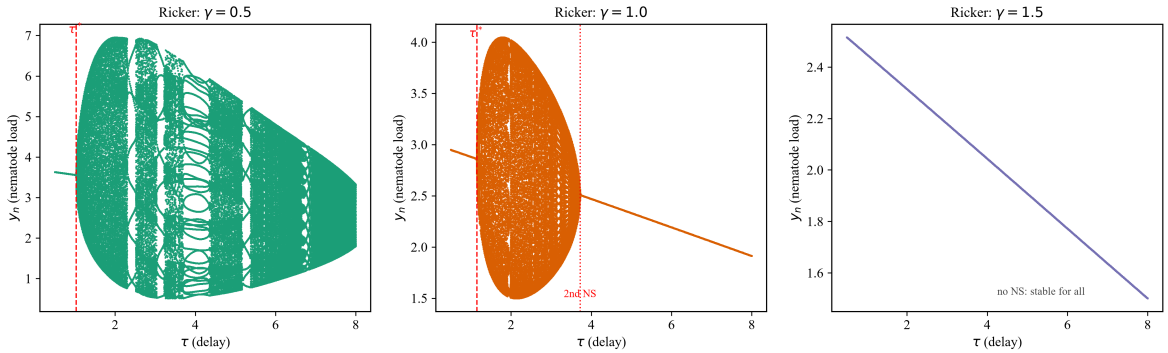

Figure 14. Ricker model: bifurcation diagrams for three levels of the adult mortality (Dark2 palette; τ is the delay, w_0 the sampled nematode load of the semidiscrete map (2.8)). Left: $\gamma = 0.5$, Neimark-Sacker threshold $\tau^* \approx 1.030$ and a wide quasiperiodic interval. Middle: $\gamma = 1.0$, the reference loss–restabilization structure ($\tau^* \approx 1.145$, secondary crossing ≈ 3.718). Right: $\gamma = 1.5$, no Neimark–Sacker bifurcation, stable for all delays.

The theoretical analysis of Section 3 shows that the stability of the positive equilibrium is governed by the product of the recruitment slope and the survival factor and that raising the adult mortality γ lowers the equilibrium w^*, weakens the feedback strength, and stabilizes the system. To quantify this mechanism, Figure 14 collects bifurcation diagrams for three levels of the adult mortality, $\gamma = 0.5, 1.0, 1.5$, with all other parameters fixed at $(\delta, b, a) = (0.1, 14.5, 0.8)$.

For the Ricker model (Figure 14), low adult mortality ($\gamma = 0.5$) makes the Neimark–Sacker threshold very small ($\tau^* \approx 1.030$) and the invariant-closed-curve interval wide: The population oscillates quasiperiodically already for a modest one-year delay, and the window of oscillatory outbreaks extends far beyond the plotted range. At the reference mortality $\gamma = 1.0$, the system exhibits the full loss–restabilization structure ($\tau^* \approx 1.145$, secondary crossing ≈ 3.718). For high mortality ($\gamma = 1.5$), the Neimark–Sacker threshold disappears, and the equilibrium is stable for every admissible delay. In silvicultural terms, the adult mortality acts as a powerful stabilization lever for overcompensatory (Ricker-type) recruitment: Raising γ from 1.0 to 1.5, for example, through adult trapping, natural-enemy release, or chemical control of the emerging vector beetles removes the oscillatory outbreak regime altogether.

3.12. Further parameter scans

The mortality scan of Section 3.11 varied the adult mortality γ. The same type of bifurcation structure is examined here under the immature mortality δ, keeping the same reference set $(\gamma, \delta, b, a) = (1, 0.1, 14.5, 0.8)$ as the middle panel of the scan.

For the Ricker model (Figure 15), the immature mortality δ controls the survival factor $e^{-\delta\tau}$ in the same qualitative way as γ. At low mortality ($\delta = 0.05$), the Neimark–Sacker threshold is as small as

$\tau^* \approx 1.024$ and the second crossing is postponed to ≈ 7.561: The quasi-periodic outbreak window is very wide, so even a modest delay keeps the system in sustained oscillation. At the reference value ($\delta = 0.10$) the full loss–restabilization structure ($\tau^* \approx 1.141$, second crossing ≈ 3.720) appears, whereas at high mortality ($\delta = 0.20$) , the Neimark–Sacker bifurcation disappears, and the equilibrium is stable for all delays. Ecologically, mortality acting on the immature stage, such as soil treatment, inundative release of larval parasitoids, or control of the juvenile vector stages, is therefore a stabilization lever of the same rank as the adult mortality for overcompensatory recruitment, and low immature mortality is one of the preconditions for the Ricker-type outbreak regime.

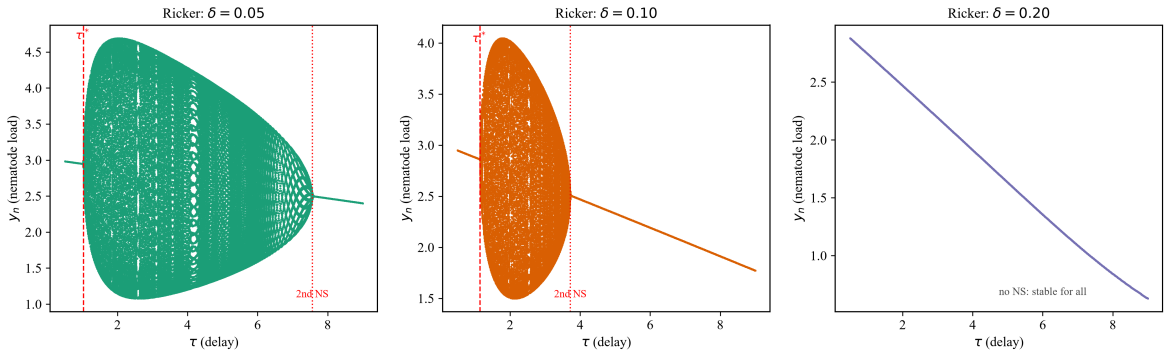

Figure 15. Ricker model: bifurcation diagrams for three levels of the immature mortality (Dark2 palette). Left: $\delta = 0.05$, Neimark–Sacker threshold $\tau^* \approx 1.024$ and a wide quasi-periodic interval (second crossing ≈ 7.561). Middle: $\delta = 0.10$, reference loss–restabilization structure ($\tau^* \approx 1.141$, second crossing ≈ 3.720). Right: $\delta = 0.20$, no Neimark–Sacker bifurcation, stable for all delays.

4. The Beverton–Holt model

4.1. The Beverton–Holt map

Repeating the piecewise-constant-arguments construction of Section 2 with $f(w) = bw/(1 + aw)$ in place of $f(w) = bwe^{-aw}$, the delayed source term (2.4) becomes

$$C_n := \tau\, e^{-\delta\tau} f(\eta(n-1)) = \tau\, e^{-\delta\tau}\, \frac{b\,\eta(n-1)}{1 + a\,\eta(n-1)}, \tag{4.1}$$

and the two-dimensional semidiscrete system (2.8) takes the form

$$\begin{cases} x(n+1) = y(n), & A_n = -\gamma\tau - \tau\, \dfrac{y(n)}{1 + y(n)^2}, \\ y(n+1) = y(n)\, e^{A_n} + C_n\, \dfrac{e^{A_n} - 1}{A_n}, & C_n = \tau\, e^{-\delta\tau}\, \dfrac{b\,x(n)}{1 + a\,x(n)}. \end{cases} \tag{4.2}$$

The only structural difference from the Ricker map (2.8) is that the source term C_n is now strictly increasing and concave in the delayed state $x(n)$ instead of being hump-shaped. As shown below, this single difference completely changes the bifurcation picture.

4.2. Existence and uniqueness of the Beverton–Holt equilibrium

The trivial fixed point $E_0 = (0, 0)$ always exists. A positive fixed point $E_* = (w^*, w^*)$ satisfies $w^* > 0$ and

$$\gamma + \frac{w^*}{1 + (w^*)^2} = \frac{\mathrm{e}^{-\delta\tau}\, b}{1 + a\, w^*}. \tag{4.3}$$

With the basic reproduction number $R_0 := \dfrac{b}{\gamma}\mathrm{e}^{-\delta\tau}$ and the auxiliary function $\varphi(w) := \dfrac{\mathrm{e}^{-\delta\tau} b}{1 + aw} - \gamma - \dfrac{w}{1 + w^2}$, we have the following:

Theorem 4.1. (i) *A positive fixed point exists if and only if $R_0 > 1$, that is $\tau < \tau_0 := \delta^{-1} \ln(b/\gamma)$.* (ii) *If in addition, $\mathrm{e}^{-\delta\tau} b \geq a$, the positive fixed point is unique. For the parameters used below ($\gamma = 1$, $\delta = 0.1$, $b = 14.5$, $a = 0.8$) this condition holds for every $\tau < \tau_0$ because $\mathrm{e}^{-\delta\tau} b > \gamma = 1 > a$.*

Proof. (i) $\varphi(0^+) = \mathrm{e}^{-\delta\tau} b - \gamma$. If $R_0 \leq 1$ then $\varphi(0^+) \leq 0$; one checks that φ then has no positive zero. If $R_0 > 1$, $\varphi(0^+) > 0$ when $\varphi(\infty) = -\gamma < 0$, so at least one positive zero exists. (ii) For $w \geq 1$, $\varphi'(w) = -\dfrac{\mathrm{e}^{-\delta\tau} ba}{(1 + aw)^2} + \dfrac{w^2 - 1}{(1 + w^2)^2}$. Because $(w^2 - 1)(1 + aw)^2 < a(1 + w^2)^2$ for $w \geq 1$, the condition $\mathrm{e}^{-\delta\tau} b \geq a$ implies $\varphi'(w) < 0$ for all $w \geq 1$, where as $\varphi' < 0$ on $(0, 1)$ is immediate; hence, φ is strictly decreasing on $(0, \infty)$ and the positive zero is unique. □

Remark 4.2. *Unlike the Ricker case, where* (3.1) *may admit multiple positive solutions and associated multistability, the monotonically saturating Beverton–Holt function yields at most one positive fixed point (two are possible only if $\mathrm{e}^{-\delta\tau} b < a$, which does not occur in the parameter range considered here). This already indicates that the Beverton–Holt model cannot exhibit the Allee-type bistability found in Ricker type outbreak models.*

4.3. The negative-determinant theorem

At the positive fixed point E_*, the Jacobian of (4.2) is

$$J = \begin{pmatrix} F_u & F_v \\ 1 & 0 \end{pmatrix}, \tag{4.4}$$

where, with $A = -\gamma\tau - \tau w^*/(1 + (w^*)^2)$ and $C = \tau \mathrm{e}^{-\delta\tau} b w^*/(1 + aw^*)$,

$$\begin{aligned} F_u &= \mathrm{e}^A + w^* \mathrm{e}^A A' + C\, \frac{\mathrm{e}^A(A - 1) + 1}{A^2}\, A', \qquad A' = -\tau\, \frac{1 - (w^*)^2}{(1 + (w^*)^2)^2}, \\ F_v &= \frac{\tau\, \mathrm{e}^{-\delta\tau}\, b}{(1 + aw^*)^2}\, \frac{\mathrm{e}^A - 1}{A} > 0. \end{aligned} \tag{4.5}$$

The characteristic polynomial of the Jacobian (4.4) is therefore obtained from $\det(\lambda I - J) = 0$, that is

$$P(\lambda) := \lambda^2 - \mathrm{tr}J\, \lambda + \det J = \lambda^2 - F_u\, \lambda - F_v = 0; \tag{4.6}$$

with trace and determinant

$$\mathrm{tr}J = F_u, \qquad \det J = -F_v. \tag{4.7}$$

Consequently, the Jury quantities (4.10) below take the explicit form

$$P(1) = 1 - \mathrm{tr}J + \det J = 1 - F_u - F_v, \qquad P(-1) = 1 + \mathrm{tr}J + \det J = 1 + F_u - F_v. \tag{4.8}$$

Theorem 4.3 (Negative-determinant theorem)**.** *For every $a > 0$ and every $\tau > 0$ such that the positive fixed point E_* exists, the Jacobian determinant satisfies*

$$\det J = -F_v = -\frac{\tau\, \mathrm{e}^{-\delta\tau}\, b}{(1 + aw^*)^2}\, \frac{\mathrm{e}^A - 1}{A} < 0. \tag{4.9}$$

Consequently, the characteristic polynomial $\lambda^2 - \mathrm{tr}J\,\lambda + \det J = 0$ has discriminant $\Delta = (\mathrm{tr}J)^2 - 4\det J > 0$, and both eigenvalues are always real with opposite signs, $\lambda_1 > 0 > \lambda_2$.

Proof. $F_v > 0$ because $(1 + aw^*)^2 > 0$ and $(\mathrm{e}^A - 1)/A > 0$ (recall $A < 0$); hence, $\det J = -F_v < 0$. The discriminant claim follows from $4\det J < 0$. □

Corollary 4.4 (Exclusion of the Neimark–Sacker bifurcation)**.** *Under the Beverton–Holt recruitment function, a Neimark–Sacker bifurcation of the positive fixed point* cannot occur *for any $a > 0$: A Neimark–Sacker bifurcation requires a conjugate pair of eigenvalues crossing the unit circle, in particular,* $\det J = |\lambda|^2 = 1 > 0$*, which contradicts* (4.9)*. The map is orientation-reversing in the sense that the product of the two local multipliers is always negative.*

This is the sharpest structural contrast with the Ricker model of Section 3, where $F_v \propto \mathrm{e}^{-aw^*}(1 - aw^*)$ changes sign, and $\det J > 0$ for $aw^* > 1$, so that the Neimark–Sacker bifurcation at $\tau^* \approx 1.141$ is possible. For the Beverton–Holt model the monotonicity of the recruitment function makes $\det J < 0$ identically, so the destabilization must occur through a real multiplier, that is through a period-doubling (Flip) or a saddle-node-type boundary.

4.4. The Jury criterion and the stability interval

For a two-dimensional map, E_* is locally asymptotically stable if and only if the Jury conditions

$$P(1) := 1 - \mathrm{tr}J + \det J > 0, \qquad P(-1) := 1 + \mathrm{tr}J + \det J > 0, \qquad |\det J| < 1 \tag{4.10}$$

hold simultaneously. For the reference parameters $(\gamma, \delta, b, a) = (1, 0.1, 14.5, 0.8)$ a direct scan of $\tau \in (0, \tau_0)$ gives the following:

- $|\det J| < 1$ holds identically ($\det J$ decreases monotonically from 0 to -1);
- $P(1) > 0$ holds identically, so there is no Fold/saddle-node boundary, and the positive fixed point is unique;
- $P(-1) > 0$ holds if and only if $\tau < \tau^*_{\mathrm{flip}} \approx 22.730448$.

Theorem 4.5 (Stability interval)**.** *Under the reference parameters, the positive fixed point E_* of the Beverton–Holt semidiscrete model* (4.2) *is locally asymptotically stable for*

$$0 < \tau < \tau^*_{\mathrm{flip},} \approx 22.730448, \tag{4.11}$$

and the unique destabilization mechanism is the crossing of the real multiplier $\lambda_2 = -1$ (Flip bifurcation).

The path of the pair $(\mathrm{tr}J, \det J)$ as τ grows is verified numerically in Section 4.8 (Figure 16): It stays entirely in the half-plane $\det J < 0$, enters the Jury stability triangle near $\det J = 0$, leaves it through the $\lambda = -1$ boundary, and never approaches the $\det J = 1$ line of the Neimark–Sacker boundary.

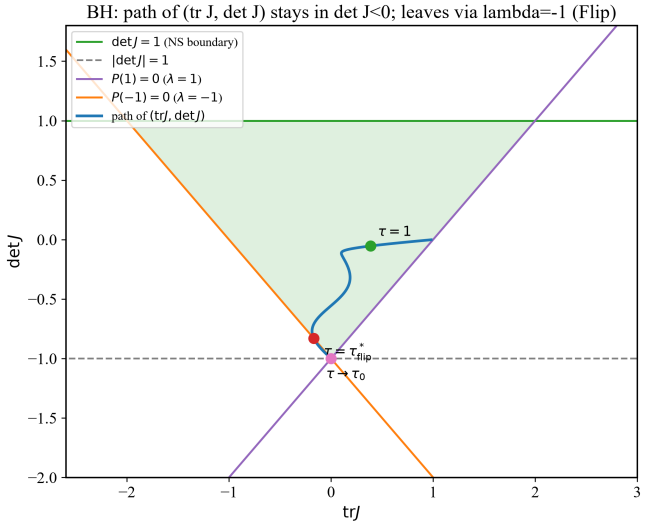

Figure 16. Beverton–Holt model: the path of $(\mathrm{tr}J, \det J)$ as τ grows (blue curve) and the Jury stability triangle (light green). The path stays entirely in the half-plane $\det J < 0$, enters the triangle near $\det J = 0$, and leaves it through the $P(-1) = 0$ boundary ($\lambda = -1$, orange line), so only a Flip bifurcation is possible; the $\det J = 1$ line (green) of the Neimark–Sacker boundary is never reached.

4.5. *Supercriticality of the Flip bifurcation*

At $\tau = \tau^*_{\mathrm{flip}}$, one has

$$w^* \approx 0.255604, \qquad \mathrm{tr}J \approx -0.169768, \qquad \det J \approx -0.830232, \qquad \lambda_2 = -1. \tag{4.12}$$

The transversality condition $\dfrac{\mathrm{d}}{\mathrm{d}\tau}P(-1)\Big|_{\tau^*} > 0$ is confirmed numerically, so a Flip bifurcation takes place. To determine its criticality, we measure the amplitude of the bifurcating period-two orbit; the resulting square-root scaling is verified numerically in Section 4.8 (Figure 17):

$$\mathrm{Amp} \approx \kappa \sqrt{\tau - \tau^*_{\mathrm{flip},}}, \qquad \kappa \approx 0.311, \tag{4.13}$$

and the period-two orbit is stable for $\tau > \tau^*_{\mathrm{flip}}$. Hence, the Flip bifurcation is supercritical: Crossing τ^*_{flip} destabilizes E_* and simultaneously creates a stable period-two orbit whose amplitude grows with the square root of the distance from the threshold, in complete analogy with the supercritical Neimark–Sacker bifurcation of the Ricker model (where the amplitude grows as $2.22\sqrt{\tau - \tau^*}$).

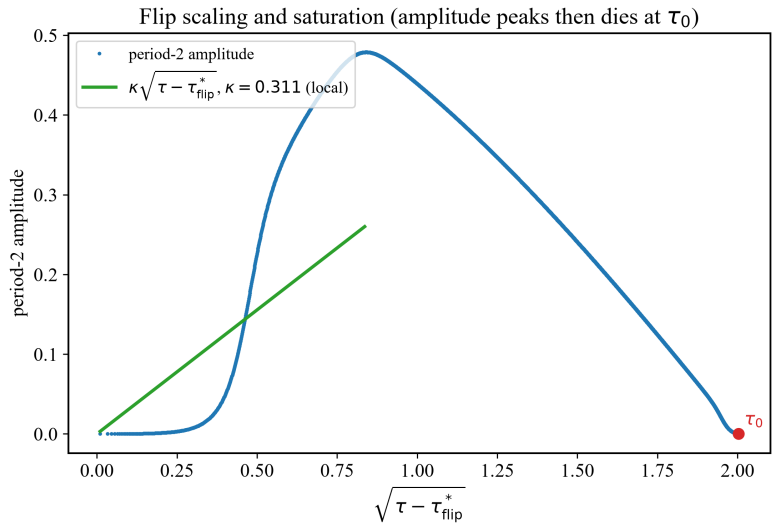

Figure 17. Beverton-Holt model: amplitude of the period-two orbit versus $\sqrt{\tau - \tau^*_{\text{flip}}}$. Locally, ($\tau - \tau^* \lesssim 0.7$) the square-root scaling with $\kappa \approx 0.311$ holds, confirming supercriticality; away from the threshold, the amplitude saturates, reaches a maximum near $\tau \approx 23.5$, and then decays to zero as $\tau \to \tau_0$, where the period-two orbit dies out together with the positive fixed point.

4.6. The transcritical bifurcation at $R_0 = 1$

When $\tau = \tau_0 = \delta^{-1} \ln(b/\gamma) \approx 26.74$, the basic reproduction number equals one, $w^*(\tau) \to 0^+$, and the positive fixed point E_* merges with the trivial extinction state E_0 (this is the $\lambda_1 = +1$, $P(1) = 0$ boundary). Stability is exchanged: Numerical evaluation of the Jury conditions at E_0 (Table 2) shows that E_0 is locally asymptotically stable for $\tau > \tau_0$ and unstable for $\tau < \tau_0$. Thus, $\tau = \tau_0$ is a transcritical bifurcation point at which the persistence-extinction transition of the population occurs.

Table 2. Beverton–Holt model: Jury quantities at the trivial fixed point $E_0 = (0, 0)$ for $\tau > \tau_0$ (tr$J \to 0$, hence, $P(1) = P(-1)$).

τ	tr$J$	det J	$P(1)$	$P(-1)$	Status
27.0	1.9×10^{-12}	−0.9745	0.0255	0.0255	stable
28.0	6.9×10^{-13}	−0.8817	0.1183	0.1183	stable
30.0	9.4×10^{-14}	−0.7219	0.2781	0.2781	stable
35.0	6.3×10^{-16}	−0.4379	0.5621	0.5621	stable
40.0	4.2×10^{-18}	−0.2656	0.7344	0.7344	stable

4.7. Absence of chaotic dynamics in the Beverton–Holt map

As in the Ricker case, chaotic dynamics is absent for the Beverton–Holt model. The maximal Lyapunov exponent satisfies $L_{\max} \leq 0$ for all $\tau \in (0, \tau_0)$ (Figure 18 in Section 4.8), so the long-time dynamics is either the stable equilibrium or the stable period-two orbit. Moreover, because det $J < 0$ (Theorem 4.3) , the eigenvalues are always real with opposite signs, so no oscillatory complex pair can ever cross the unit circle; the only possible transition is the Flip bifurcation of Theorem 4.5, after

which the system settles on an alternating period-two orbit. No period-doubling cascade, and hence no chaotic attractor, is possible.

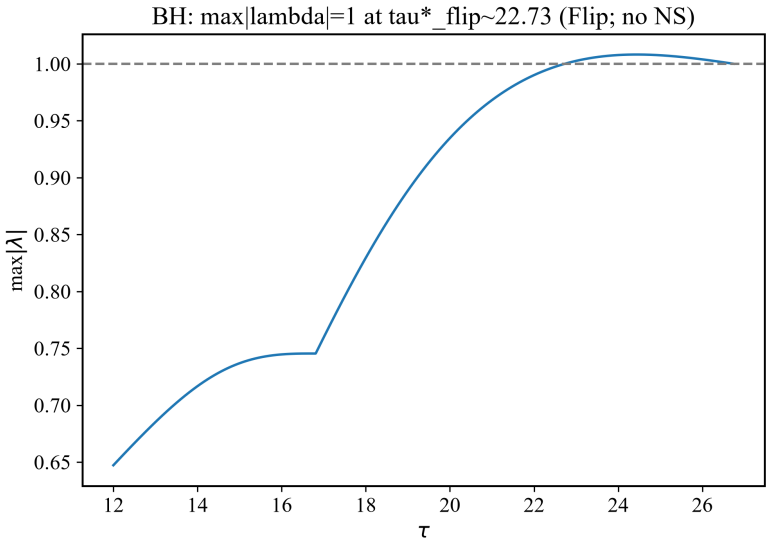

Figure 18. Beverton–Holt model: maximal Lyapunov exponent spectrum (Benettin algorithm with orbit evolution and continuation initial data). The maximal exponent satisfies $L_{\max} \leq 0$ for all $\tau \in (0, \tau_0)$: The dynamics is either a stable equilibrium or a stable period-two orbit, and chaotic behavior is absent.

4.8. Numerical verification for the Beverton–Holt model

Throughout this subsection, the parameters are fixed at $(\gamma, \delta, b, a) = (1, 0.1, 14.5, 0.8)$ unless stated otherwise, and the map is read as a generational model of the pine wilt system: x_n is the nematode load carried by the emerging vector beetles (*Monochamus alternatus*) of generation n, τ is the one-year developmental delay imposed by the beetle life cycle, δ the adult mortality, b the per-capita reproductive output, and a the intensity of density-dependent saturation in recruitment.

Figure 19 is the bifurcation diagram over the full range $\tau \in (0.5, 26.8)$ and contains the whole outbreak scenario of the system. For short beetle generations, the population settles to a constant annual level; as the delay passes $\tau^*_{\text{flip}} \approx 22.7304$ the equilibrium loses stability through a supercritical Flip bifurcation, and the population alternates between outbreak and low years; for $\tau \gtrsim 23.5$ the trough of the period-two cycle is driven close to zero, giving rise to the pulse-like oscillation; and as τ approaches $\tau_0 \approx 26.74$ the two branches merge, and the population is extinguished ($R_0 = 1$, transcritical boundary). Figure 20 magnifies the Flip region: The two emerging branches quantify the amplitude of the outbreak-suppression alternation, the upper branch being the outbreak-year peak and the lower branch the trough.

Figure 21 evaluates the Jury quantities along the equilibrium branch: $P(-1)$ crosses zero exactly at τ^*_{flip} while $\det J$ remains negative for every $\tau \in (0, \tau_0)$, confirming Corollary 4.4 that the Neimark–Sacker mechanism is structurally excluded under Beverton–Holt saturation. Ecologically this means that Beverton-Holt type recruitment cannot generate quasiperiodic slowly drifting oscillations of nematode density; sustained year-to-year oscillation, whenever it occurs, is always a period-two outbreak-suppression cycle, which considerably simplifies the early-warning indicators available to

forest managers.

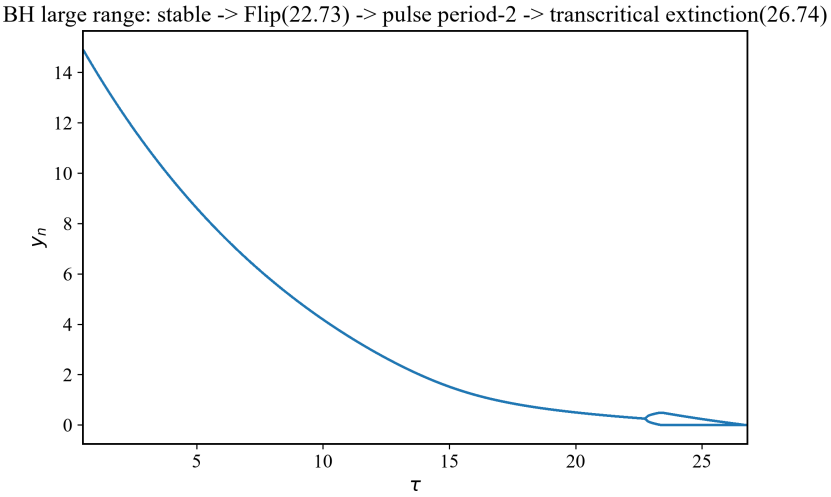

Figure 19. Beverton–Holt model: bifurcation diagram over the full range $\tau \in (0.5, 26.8)$ (Tableau blue dots). The stable equilibrium for $\tau < \tau^*_{\text{flip}} \approx 22.7304$ gives way to a stable period-two orbit after the supercritical Flip bifurcation; for $\tau \gtrsim 23.5$, the oscillation becomes pulse-like, with the lower branch driven close to zero, and the two branches merge at the transcritical boundary $\tau_0 \approx 26.74$, where the population is extinguished.

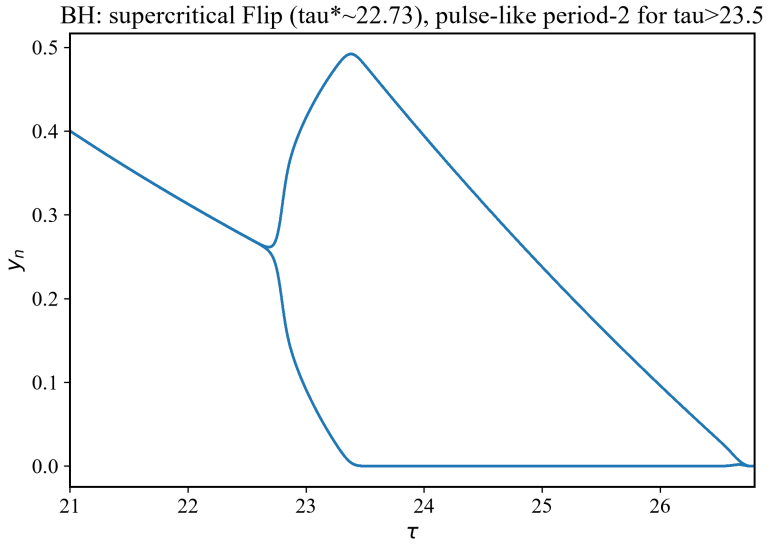

Figure 20. Beverton–Holt model: magnification of the Flip region, $\tau \in [21, 26.8]$. The supercritical Flip occurs at $\tau^*_{\text{flip}} \approx 22.7304$; the upper emerging branch is the outbreak-year peak of the period-two cycle, and the lower branch is the suppression-year trough, and both branches merge at the transcritical boundary.

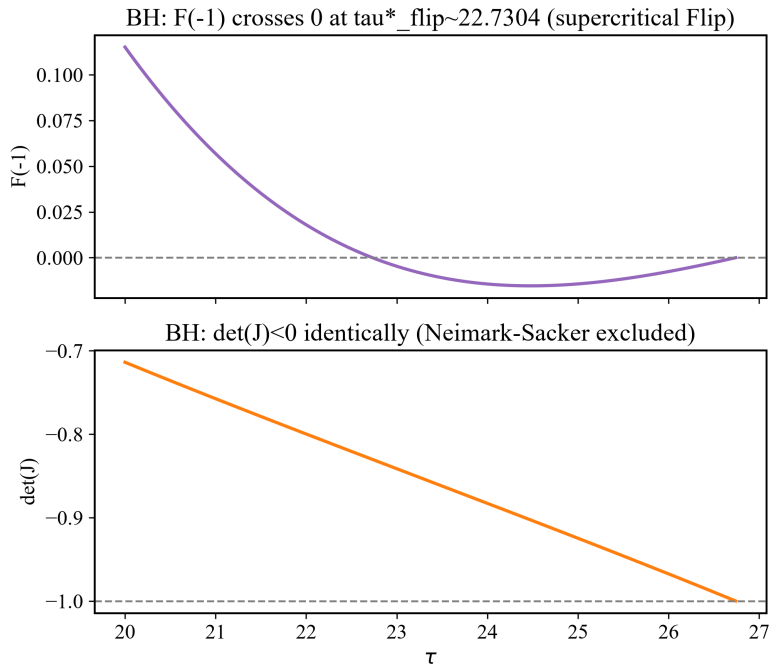

Figure 21. Beverton–Holt model: Jury verification along the equilibrium. Upper panel: $P(-1) = 1 + \mathrm{tr}J + \det J$ (purple) crosses zero at $\tau^*_{\mathrm{flip}} \approx 22.7304$, signalling the Flip bifurcation. Lower panel: $\det J$ (orange) is negative throughout $\tau \in (0, \tau_0)$, so the Neimark–Sacker bifurcation is excluded (Corollary 4.4).

The same structural exclusion is visible in the Jury triangle plane. Figure 16 shows the path of $(\mathrm{tr}J, \det J)$ as τ grows: It stays entirely in the half-plane $\det J < 0$, enters the stability triangle near $\det J = 0$, and leaves it through the $P(-1) = 0$ boundary, so only a Flip transition is possible. Moreover, the amplitude of the bifurcating period-two orbit obeys the square-root law predicted by the theory: Figure 17 confirms Amp $\approx \kappa \sqrt{\tau - \tau^*_{\mathrm{flip}}}$ with $\kappa \approx 0.311$ near the threshold, and the amplitude saturates, reaches a maximum near $\tau \approx 23.5$, and decays to zero at the transcritical boundary τ_0, where the period-two orbit dies out together with the positive fixed point.

Figure 22 collects waveforms of the current-generation state y_n of (4.2) for six representative delays. For $\tau = 15$ and $\tau = 20$, a transient perturbation decays, and the density converges to the constant equilibrium, the latter slowly because the Flip threshold is approached (critical slowing down). At $\tau = 22.73$, which is exactly the analytically predicted Flip threshold, the equilibrium is already unstable, and an incipient period-two alternation of tiny amplitude appears. For $\tau = 23.2$ the period-two outbreak–suppression cycle is fully developed, and at $\tau = 25.5$ every second generation almost vanishes before rebounding: The pulse-like pattern matches the field picture of pine wilt disease, where beetle-trapping records often show an outbreak year followed by an almost undetectable year, and the trough generation provides the natural window for sanitation felling and nematicide application. Finally, as τ approaches the transcritical boundary $\tau_0 \approx 26.74$, the pulse amplitude shrinks, and the two levels merge ($\tau = 26.5$), anticipating the extinction of the population.

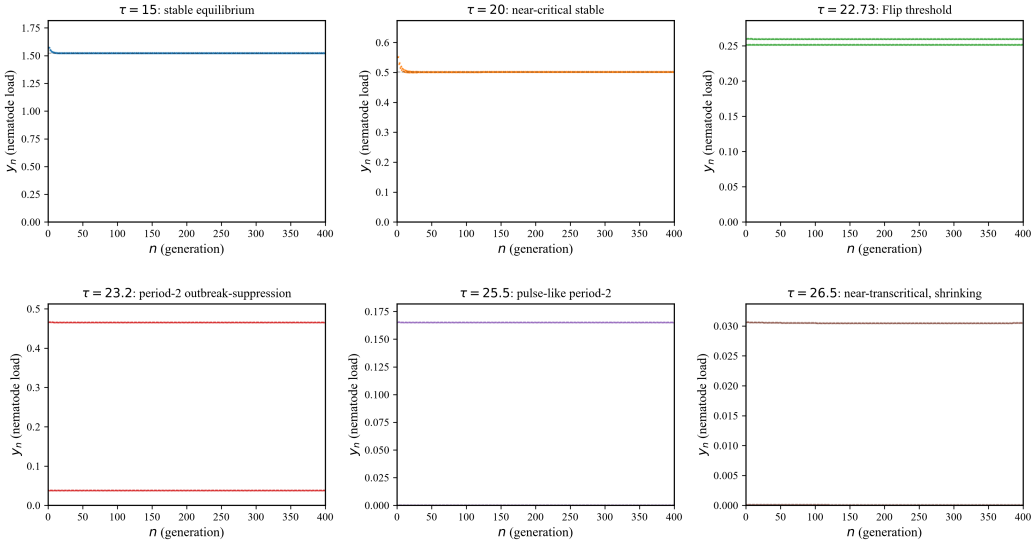

Figure 22. Beverton–Holt model: discrete-generation waveforms of the current-generation state y_n of (4.2) versus the generation index n for six representative delays (Tableau palette). Top row: $\tau = 15$ (stable equilibrium $w^* \approx 1.5221$), $\tau = 20$ (stable, near the Flip threshold), $\tau = 22.73$ (incipient period-two at the Flip threshold). Bottom row: $\tau = 23.2$ (period-two outbreak-suppression), $\tau = 25.5$ (pulse-like period-two with nearly vanishing trough), $\tau = 26.5$ (shrinking pulse near the transcritical boundary $\tau_0 \approx 26.74$).

Figure 18 is the maximal Lyapunov exponent spectrum computed by the Benettin algorithm with orbit evolution and continuation initial data. Because $L_{\max} \leq 0$ for all $\tau \in (0, \tau_0)$, the dynamics is either a stable equilibrium or a stable period-two orbit and chaos is absent: Under Beverton–Holt saturation the outbreak dynamics remains predictable, so deterministic risk forecasting for the pine wilt system is legitimate.

Finally, the dependence of the Flip threshold on the saturation parameter is shown in Figure 23 and Table 3. For fixed $(\gamma, \delta, b) = (1, 0.1, 14.5)$, $\tau^*_{\text{flip}}(a)$ exists only for sufficiently small a; for $a \gtrsim 1.5$ the positive fixed point remains stable throughout $\tau \in (0, \tau_0)$ and no oscillation occurs. Strengthening density saturation, for example through resistant pine varieties, high stand competition, or natural-enemy pressure, either postpones the onset of the oscillatory regime or removes it altogether: In silvicultural terms, enhancing intraspecific competition is a stabilizing measure that keeps the nematode-vector system in the constant annual regime.

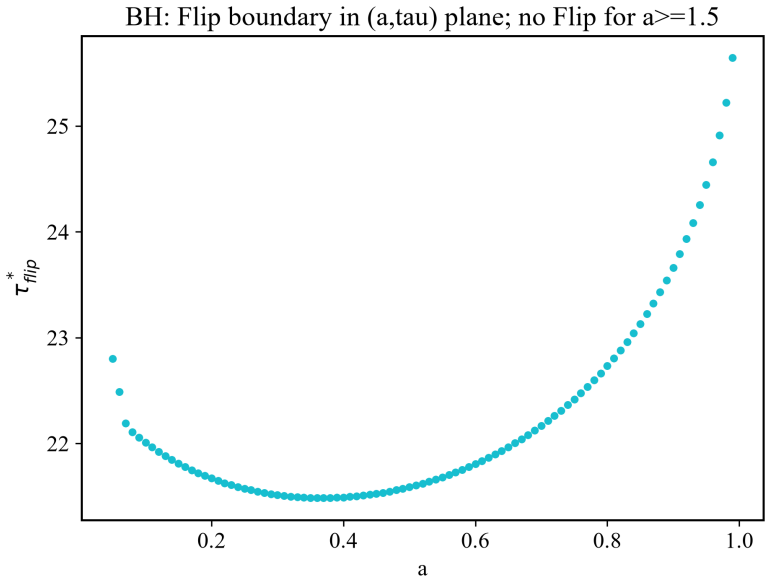

Figure 23. Beverton–Holt model: Flip threshold τ^*_{flip} versus the saturation parameter a (cyan dots). The Flip bifurcation exists only for $a \lesssim 1.5$; for $a \gtrsim 1.5$ the positive equilibrium is stable for all $\tau < \tau_0$, that is saturation suppresses the outbreak oscillation.

Table 3. Beverton–Holt model: Flip threshold τ^*_{flip} versus the saturation parameter a ($w^*(0.1)$ is the equilibrium at $\tau = 0.1$; "none" means the equilibrium is stable for all $\tau < \tau_0$).

a	0.05	0.1	0.2	0.4	0.8	1.5	2.5
$w^*(0.1)$	200.0	132.5	65.7	32.3	15.6	7.8	4.3
τ^*_{flip}	22.74	22.01	21.67	21.49	22.74	none	none

4.9. Bifurcation structure under adult mortality

The theoretical analysis of Section 4 shows that the stability of the positive equilibrium is governed by the product of the recruitment slope and the survival factor and that raising the adult mortality γ lowers the equilibrium w^*, weakens the feedback strength, and stabilizes the system. To quantify this mechanism, Figure 24 collects bifurcation diagrams for three levels of the adult mortality, $\gamma = 0.5, 1.0, 1.5$, with all other parameters fixed at $(\delta, b, a) = (0.1, 14.5, 0.8)$.

For the Beverton–Holt model (Figure 24) the same mortality scan shows a different structure. The transcritical (extinction) threshold $\tau_0 = \delta^{-1} \ln(b/\gamma)$ decreases with γ (33.67, 26.74, 22.69), whereas the Flip threshold moves from $\tau^*_{\text{flip}} \approx 24.72$ ($\gamma = 0.5$) through 22.74 ($\gamma = 1.0$) and disappears for $\gamma = 1.5$, where the equilibrium is stable for all $\tau < \tau_0$. Thus increasing the adult mortality simultaneously delays the onset of the period-two oscillation and pulls the extinction boundary closer; both effects act in the stabilizing direction so that high mortality leaves only the constant annual regime before the population is extinguished.

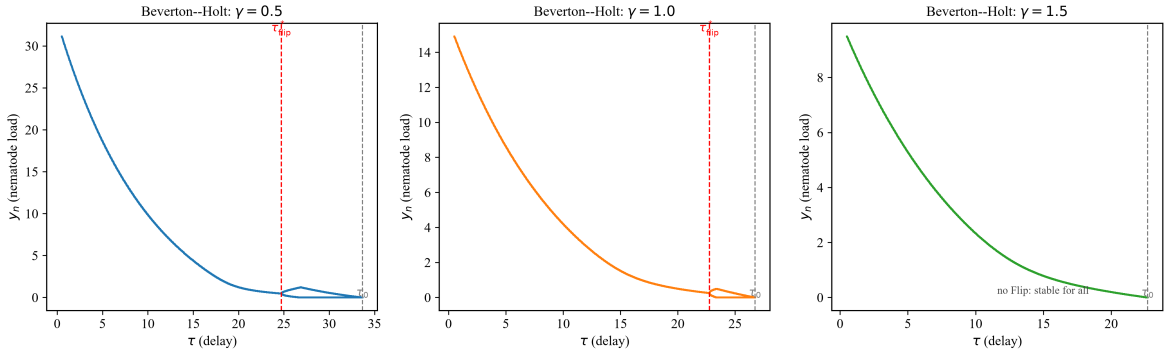

Figure 24. Beverton-Holt model: bifurcation diagrams for three levels of the adult mortality (Tableau palette). Left: $\gamma = 0.5$, Flip threshold $\tau^*_{\text{flip}} \approx 24.72$ and transcritical boundary $\tau_0 \approx 33.67$. Middle: $\gamma = 1.0$, $\tau^*_{\text{flip}} \approx 22.74$, $\tau_0 \approx 26.74$. Right: $\gamma = 1.5$, no Flip bifurcation, stable for all $\tau < \tau_0 \approx 22.69$; the transcritical boundary is marked by the gray dashed line.

4.10. Further parameter scans

The mortality scan of Section 4.9 varied the adult mortality γ. The same type of bifurcation structure is examined here under two additional system parameters, the immature mortality δ and the saturation strength a, keeping the same reference set $(\gamma, \delta, b, a) = (1, 0.1, 14.5, 0.8)$ as the middle panel of each scan.

For the Beverton–Holt model (Figure 25), the immature mortality acts as a scaling knob for the whole oscillatory-to-extinction time schedule. Both the Flip threshold and the transcritical boundary are proportional to δ^{-1}: They move from $(\tau^*_{\text{flip}}, \tau_0) \approx (45.47, 53.48)$ at $\delta = 0.05$ through $(22.74, 26.74)$ at $\delta = 0.10$ to $(11.37, 13.37)$ at $\delta = 0.20$. The relative length of the period-two window stays approximately constant, but its absolute position shrinks as mortality rises. Hence, for compensatory recruitment, increasing the immature mortality does not suppress the oscillation; it merely compresses the entire outbreak scenario into an earlier, shorter part of the delay axis.

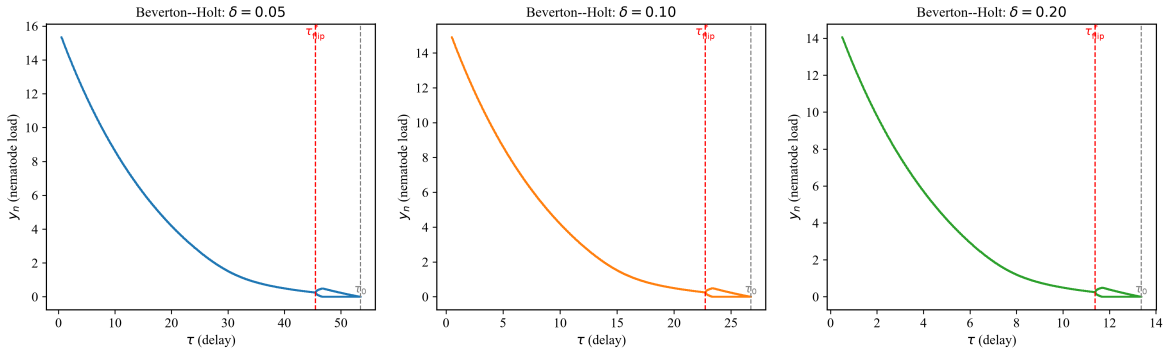

Figure 25. Beverton–Holt model: bifurcation diagrams for three levels of the immature mortality (Tableau palette). The Flip threshold and the transcritical boundary move together: $(\tau^*_{\text{flip}}, \tau_0) \approx (45.47, 53.48)$ for $\delta = 0.05$, $(22.74, 26.74)$ for $\delta = 0.10$, $(11.37, 13.37)$ for $\delta = 0.20$. The period-two window keeps its relative length but is compressed on the delay axis.

Finally, the saturation strength a acts on the Beverton–Holt model in a way that differentials the two mechanisms (Figure 26, logarithmic scale). The Flip threshold is nonmonotone in a: It first decreases

to $\tau^*_{\text{flip}} \approx 22.01$ at $a = 0.1$, then increases to 22.74 at $a = 0.8$, and disappears for $a \gtrsim 1.5$, whereas the transcritical boundary $\tau_0 = 26.74$ is independent of a. Strong saturation therefore suppresses the oscillation without changing the extinction window: Density-dependent compensation stabilizes the annual level, but the population is extinguished at the same delay as in the weakly saturating case. In management terms, saturation-enhancing measures such as resistant pine varieties, high stand competition, and natural enemy pressure eliminate the alternating outbreak–suppression cycle, yet they do not postpone the collapse induced by an excessive delay; the two phenomena are governed by two largely independent parameters.

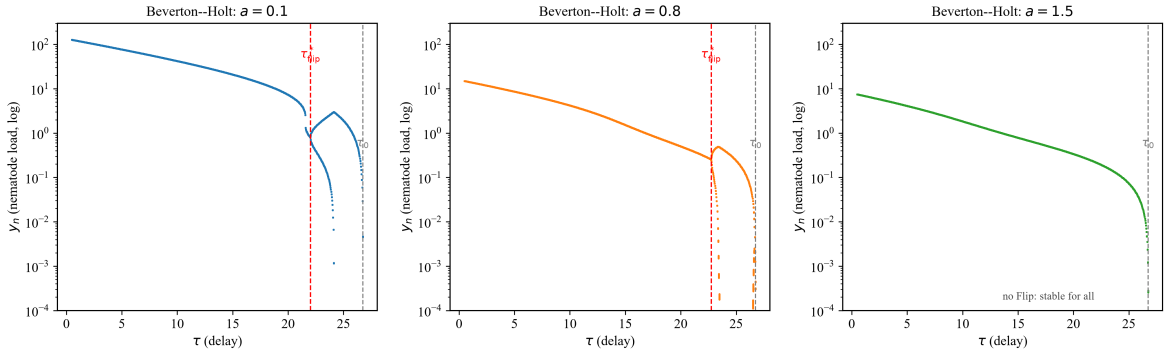

Figure 26. Beverton–Holt model: bifurcation diagrams for three levels of the saturation strength a (Tableau palette, logarithmic ordinate). Left: $a = 0.1$, Flip threshold $\tau^*_{\text{flip}} \approx 22.01$; middle: $a = 0.8$, $\tau^*_{\text{flip}} \approx 22.74$; right: $a = 1.5$, no Flip bifurcation, stable for all $\tau < \tau_0$. The transcritical boundary $\tau_0 = 26.74$ is independent of a, so saturation suppresses the oscillation without changing the extinction window.

4.11. Horizontal comparison with the Ricker model

Figure 27 places the two models side by side at the reference parameters $(\gamma, \delta, b, a) = (1, 0.1, 14.5, 0.8)$. The contrast is structural, not quantitative. The Ricker system loses stability through a conjugate pair of complex multipliers and develops an invariant closed curve: The year-to-year fluctuations appear gradually, and their amplitude grows continuously, so early-warning monitoring can detect the onset of quasiperiodic oscillations while the amplitude is still small. The Beverton–Holt system loses stability only through the real multiplier $\lambda = -1$ and develops a period-two outbreak–suppression cycle: Below the threshold, the annual level is constant, whereas beyond it the population alternates between an outbreak year and a suppressed year without an intermediate regime. The horizontal comparison therefore yields a testable field criterion. If trapping records show continuous, aperiodic year-to-year oscillations with slowly growing amplitude, an overcompensatory (Ricker) mechanism is the more appropriate descriptor; if the records show a sharp transition to strictly alternating outbreak–suppression years, a compensatory (Beverton–Holt) mechanism with strong saturation is at work. Moreover, the two stabilization measures differ in their range of action: Raising the adult mortality is the more efficient lever for Ricker type recruitment (it eliminates the oscillation already at $\gamma = 1.5$), whereas strengthening density-dependent saturation removes the oscillation for Beverton–Holt-type recruitment ($a \gtrsim 1.5$); combining adult mortality control with saturation-enhancing measures (resistant varieties, high stand competition) therefore provides two

largely independent stabilizing lines of defense against pine wilt outbreaks.

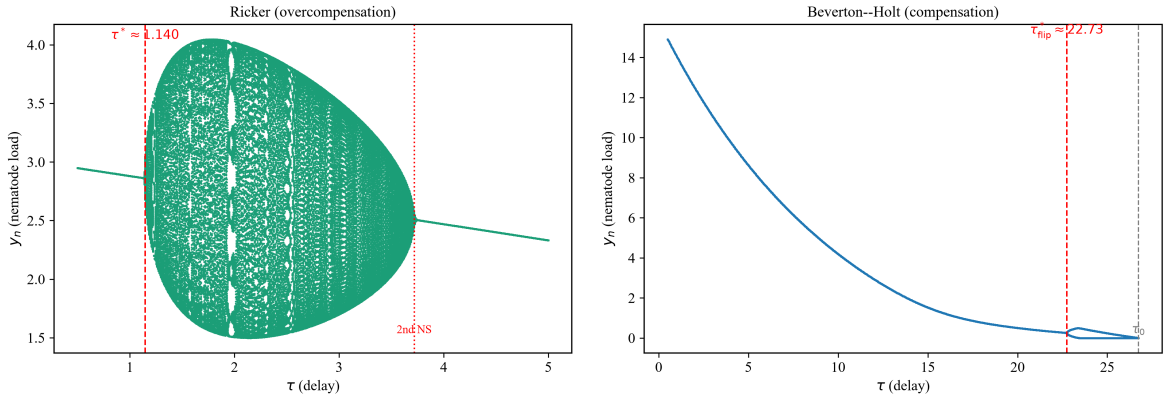

Figure 27. Horizontal comparison at the reference parameters $(\gamma, \delta, b, a) = (1, 0.1, 14.5, 0.8)$. Left: The Ricker model loses stability via a conjugate complex pair at $\tau^* \approx 1.140$ and is restabilized at the secondary Neimark-Sacker crossing ≈ 3.718, with an invariant closed curve in between. Right: The Beverton–Holt model loses stability via $\lambda = -1$ at $\tau^*_{\text{flip}} \approx 22.73$, producing a period-two outbreak-suppression cycle, followed by the transcritical extinction at $\tau_0 \approx 26.74$; no Neimark–Sacker mechanism exists.

Taken together, the parametric scans of the Ricker and Beverton–Holt models provide a complete picture of the three stabilization levers available against pine wilt outbreaks: the adult mortality γ, the immature mortality δ, and the density-dependent strength a (or its Ricker analog For overcompensatory (Ricker type) recruitment, any of the two mortality levers can remove the quasi-periodic oscillation entirely, and the saturation strength controls the onset of the oscillation; for compensatory (Beverton–Holt type) recruitment, only the saturation strength can eliminate the period-two cycle, whereas the mortalities merely rescale the outbreak scenario on the delay axis. The choice of the control measure should therefore be matched to the recruitment mechanism inferred from field trapping records, as discussed in Section 5.

5. Ecological comparison of the two recruitment mechanisms and guidance for model selection

The two recruitment mechanisms analysed in Sections 3 and 4 differ not only in their mathematical structure but, through it, in the entire outbreak scenario they predict for the pine wilt system. Figure 28 summarizes the central message of this comparison: The shape of the recruitment function fixes both the outbreak regime and the effective control lever. The Ricker overcompensatory form generates Neimark–Sacker quasiperiodic waves that are suppressed by mortality control, whereas the Beverton–Holt compensatory form generates pulse-like period-two outbreaks that are suppressed by strengthening density saturation. In this section, we turn the mathematical results of Sections 3 and 4 into a practical, ecology-oriented comparison: which recruitment mechanism is at work, what its observable fingerprint is, and which control measure it makes effective. The quantitative evidence behind each statement is provided in Section 3.8 and Section 4.8.

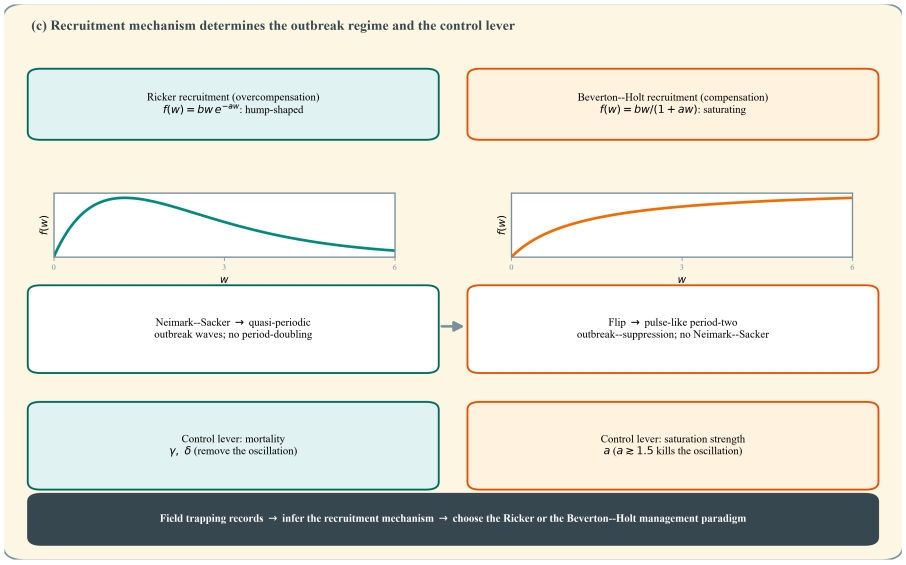

Figure 28. The two recruitment mechanisms, their recruitment functions, their bifurcation consequences (Neimark–Sacker quasiperiodic waves for Ricker; Flip pulse-like period-two outbreak-suppression for Beverton–Holt) and the corresponding control levers (mortality γ, δ versus saturation strength a), with the field criterion for the choice of the management paradigm.

5.1. *Structural comparison of the two models*

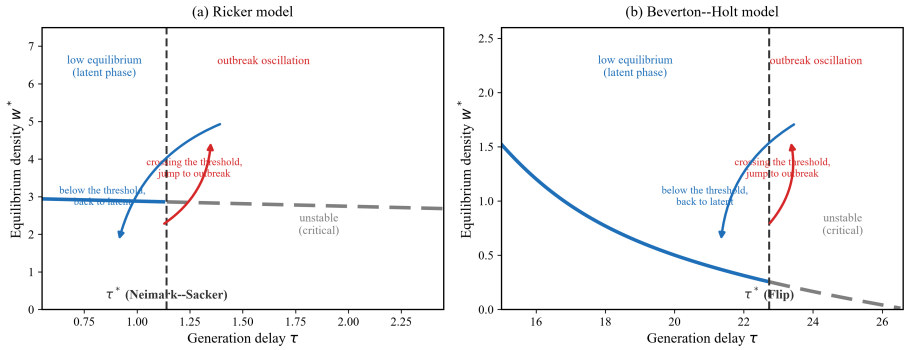

Figure 29. Equilibrium density w^* versus the generation delay τ for (a) the Ricker and (b) the Beverton–Holt recruitment versions of the semidiscrete pine wilt model; all curves are computed from the semidiscrete maps with $(\gamma, \delta, b, a) = (1, 0.1, 14.5, 0.8)$. In each panel, the blue branch is the stable low-density equilibrium of the latent phase; the grey dashed branch is the unstable continuation; and the red envelope is the outbreak oscillation created at the threshold τ^*: Neimark–Sacker at $\tau^* \approx 1.141$ in (a), period-doubling at $\tau^*_{\text{flip}} \approx 22.73$ in (b). Crossing the threshold drives the system into the outbreak regime, whereas falling back below it restores the latent regime; the arrows summarize this regime shift in the style of the classical hysteresis diagram of forest-pest outbreaks.

Figure 29 visualizes the equilibrium branches of the two models as functions of the generation delay τ, and Table 4 summarizes the qualitative differences between the Ricker and Beverton–Holt versions of the semidiscrete pine wilt model, all obtained with the same reference parameters $(\gamma, \delta, b) = (1, 0.1, 14.5)$ and $a = 0.8$.

Table 4. Comparison of the Ricker and Beverton–Holt recruitment versions of the semidiscrete pine wilt model.

	Ricker $f(w) = bwe^{-aw}$	Beverton–Holt $f(w) = \dfrac{bw}{1+aw}$
Shape	hump-shaped, overcompensatory	increasing, bounded, compensatory
$f'(w)$ sign	changes at $w = 1/a$	always positive
Positive fixed point	unique for $R_0 > 1$; more may appear elsewhere	unique for $R_0 > 1$ when $e^{-\delta\tau}b \geq a$
$\det J$ at E_*	sign changes ($\det J > 0$ if $aw^* > 1$)	always negative
Destabilization	supercritical Neimark–Sacker	supercritical period-doubling (Flip)
Critical delay	$\tau^* \approx 1.141$	$\tau^*_{\text{flip}} \approx 22.73$
Bifurcating object	invariant closed curve, quasi-periodic	period-two orbit, possibly pulse-like
Amplitude law	$2.22\sqrt{\tau - \tau^*}$	$0.311\sqrt{\tau - \tau^*_{\text{flip}}}$
Period-doubling	impossible (proved)	is the unique destabilization mechanism
Extinction boundary	$\tau_0 \approx 26.74$ (Fold)	$\tau_0 \approx 26.74$ (transcritical)
Chaos	absent; $L_{\max} \leq 0$	absent; $L_{\max} \leq 0$

Three structural facts are of general value beyond the particular model studied here. First, the *monotonicity of the recruitment function* controls the sign of the Jacobian determinant of the semidiscrete map: For any increasing recruitment function, such as Beverton–Holt, the delayed source term C_n has positive derivative; hence $\det J < 0$ and Neimark–Sacker bifurcations are structurally excluded. Second, the *hump shape* of the recruitment function (Ricker, Hassell-May type curves with overcompensation) is necessary for the appearance of the Neimark–Sacker bifurcation in the present class of models. Third, the bifurcation that replaces Neimark–Sacker is the period-doubling bifurcation, whose supercritical version produces stable alternating (period-two) oscillations instead of invariant closed curves.

5.2. Global boundedness and the single-attractor property

The global dynamical picture obtained above for the semidiscrete map is fully consistent with the global results established by Shu et al. [10] for the underlying continuous model (1.1) in the spatially homogeneous case $d = 0$: The delay reaction diffusion system admits globally existing, uniformly bounded solutions, and the maturation delay acts as the organizing bifurcation parameter, with a stable spatially homogeneous steady state for small delays and a global Hopf branch of periodic solutions emanating from it when the delay crosses the critical value. The boundedness and the absence of blow-

up in the continuous model are therefore inherited by the semidiscrete map: The piecewise-constant discretization preserves the global existence of solutions and confines every orbit to a bounded region of the positive quadrant, whatever the initial condition.

Figure 30 verifies this global property numerically. For each model, six widely separated initial conditions w_0 (ranging from a small fraction to several multiples of the equilibrium w^*) are iterated under the semidiscrete map. In the subcritical regime, every orbit converges to the unique positive equilibrium w^* Panels (a) and (c)); in the supercritical regime, every orbit is attracted to the same invariant closed curve Panel (b)) or to the same period-two cycle (panel (d)). In all cases, the orbits remain bounded, no orbit escapes to infinity, and no second attractor is observed, which corroborates the global-dynamics results of [10] at the discrete level. The absence of chaotic behavior is confirmed by the maximal Lyapunov exponent spectra reported in Sections 3.8 and 4.8: $L_{\max} \leq 0$ throughout, so the semidiscrete pine wilt map never exhibits sensitive dependence on initial conditions, in agreement with the prediction of [10] that the present class of forest-pest-type models does not support chaotic regimes.

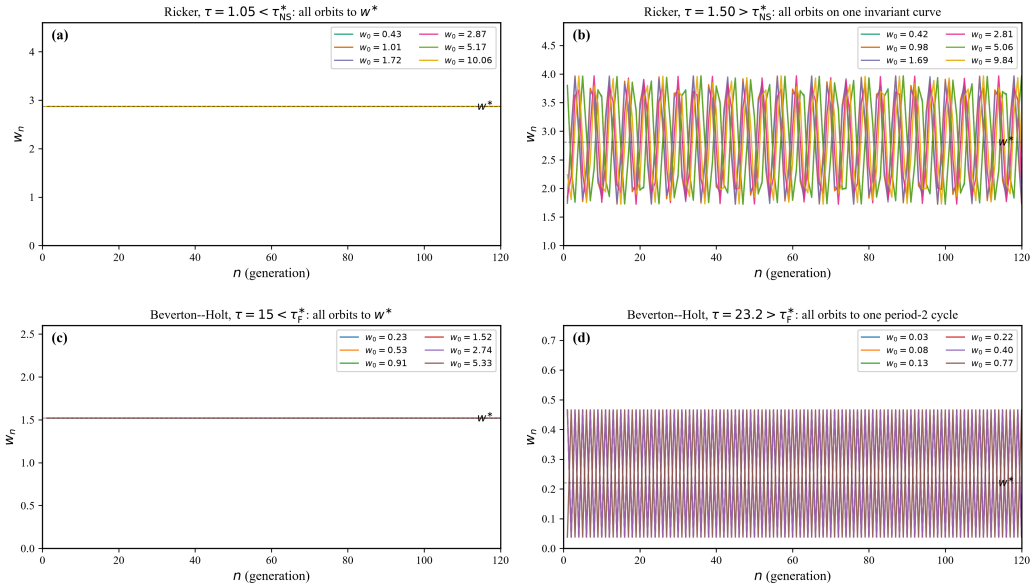

Figure 30. Global boundedness and the single-attractor property of the semidiscrete pine wilt map. Six widely separated initial conditions w_0 are iterated for each model. (a) Ricker, $\tau = 1.05 < \tau^*_{\mathrm{NS}}$: All orbits converge to the unique positive equilibrium w^*. (b) Ricker, $\tau = 1.50 > \tau^*_{\mathrm{NS}}$: All orbits are attracted to the same invariant closed curve. (c) Beverton–Holt, $\tau = 15 < \tau^*_{\mathrm{flip}}$: All orbits converge to w^*. (d) Beverton–Holt, $\tau = 23.2 > \tau^*_{\mathrm{flip}}$: All orbits are attracted to the same period-two cycle. All orbits remain bounded, and no second attractor is observed, corroborating the global boundedness results of [10] for the continuous model and confirming the absence of chaos in the semidiscrete map.

5.3. Biological guidance

The analysis provides the following practically oriented recommendations for choosing the recruitment function in delay-differential and semidiscrete models of insect outbreaks and fisheries, summarized visually in Figure 31.

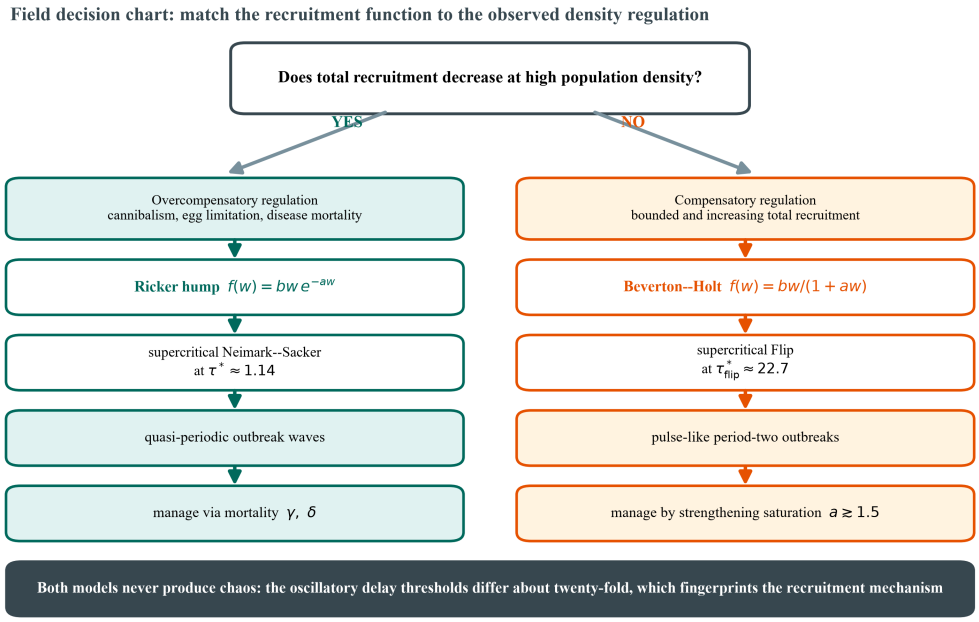

Figure 31. Field decision chart matching the recruitment function to the observed density regulation. Overcompensation selects the Ricker hump and its Neimark–Sacker waves, compensation selects the Beverton–Holt saturating form and its period-two pulses, and the twenty-fold difference in destabilizing delay fingerprints the mechanism; neither regime is chaotic.

(G1) Overcompensation calls for the Ricker form. When total recruitment decreases at high density, as driven by strong cannibalism, egg limitation, or disease-induced mortality, the Ricker form or another hump-shaped curve is the correct choice. The model then predicts a supercritical Neimark–Sacker bifurcation: Once the maturation delay exceeds $\tau^* \approx 1.14$, the equilibrium gives way to quasiperiodic oscillations on an invariant closed curve, with neither period-doubling nor chaos. Management should therefore expect smooth, rotational outbreak cycles.

(G2) Compensation calls for the Beverton–Holt form. When density regulation is purely compensatory, with per-capita recruitment decreasing while total recruitment stays bounded and increasing as in many fish stocks and strongly regulated insect populations, the Beverton–Holt form is appropriate. The model then predicts that Neimark–Sacker bifurcations *cannot* occur; instead, a supercritical Flip bifurcation at the much larger delay $\tau^*_{\text{flip}} \approx 22.7$ produces alternating period-two outbreaks that, for large delay, become pulse-like near-extinction generations. Failing to observe quasi-periodic oscillations in field data does not mean that delay effects are absent; it may simply reflect a compensatory recruitment mechanism whose period-two cycles appear only at very long maturation times.

(G3) The destabilization delay fingerprints the recruitment mechanism. Under identical parameters, the Ricker model loses stability at $\tau^* \approx 1.14$, whereas the Beverton–Holt model stays stable until $\tau^*_{\text{flip}} \approx 22.7$, about twenty times larger. Estimates of the maturation delay at which field outbreaks turn oscillatory can therefore discriminate overcompensatory from compensatory recruitment.

(G4) Saturation strength is a stabilizing factor. For Beverton–Holt recruitment, increasing the saturation parameter a shrinks and eventually removes the oscillatory regime, with no Flip at all

once $a \gtrsim 1.5$. Populations with strong density-dependent saturation are structurally stable and can be managed by the classical equilibrium paradigm; populations with weak saturation require non-equilibrium period-two management protocols.

(G5) Both models exclude chaos. Across the parameter ranges studied here, the maximal Lyapunov exponent is nonpositive for both recruitment functions: The semidiscrete dynamics stays quasiperiodic for Ricker or period-two for Beverton–Holt, and never chaotic. The robust message for outbreak forecasting is that management should target the delay threshold and the oscillation amplitude, not chaotic unpredictability.

6. Conclusions

To make the conclusions of this paper tangible, Figure 32 recalls the pine wilt transmission cycle that underlies the model: The vector beetles (*Monochamus* spp.) feed on the pine canopy, the nematode load w_n develops in the tree, and the maturation delay τ enters as the delayed source $e^{-\delta\tau} f(w_{n-1})$ of the next generation; the numbered steps 1–4 complete the cycle. Figure 33 shows the modeling pipeline of this paper: The continuous model with $d = 0$ is converted by the piecewise-constant-arguments method into the two-dimensional map $(x_{n+1}, y_{n+1}) = F(x_n, y_n)$, whose stability is decided by the Jury criterion.

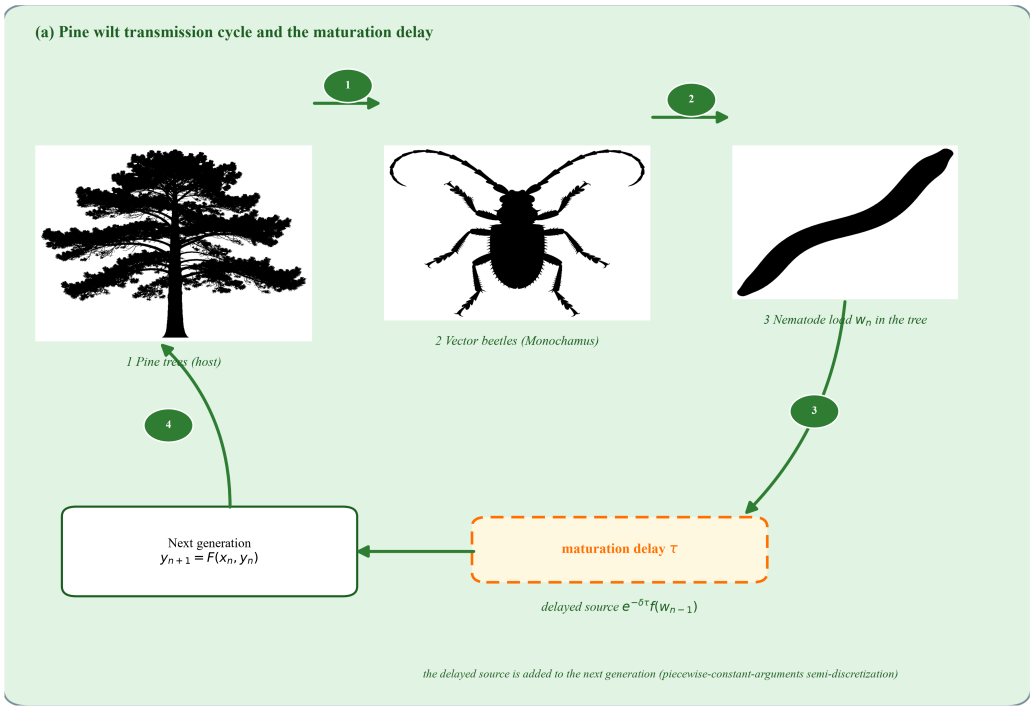

Figure 32. The pine wilt transmission cycle and the maturation delay τ: The silhouettes of the host pine, the vector beetle (*Monochamus* spp.) and the pinewood nematode, the numbered transmission steps 1–4, and the delayed source $e^{-\delta\tau} f(w_{n-1})$ added to the next generation.

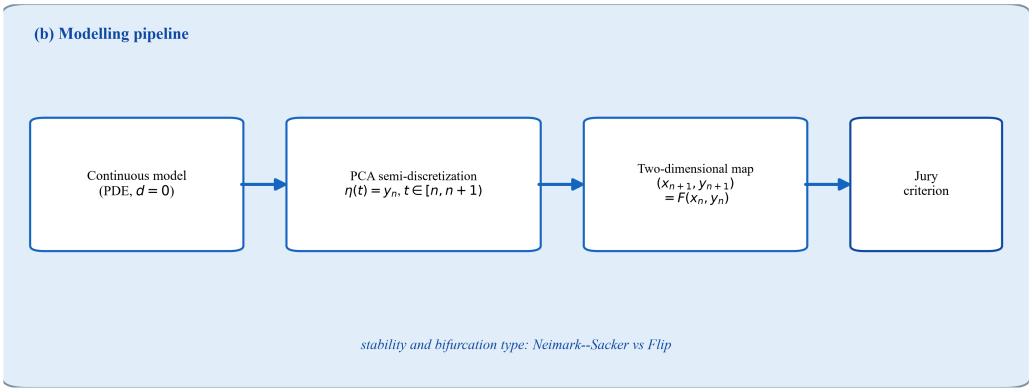

Figure 33. Modeling pipeline from the continuous model ($d = 0$) to the two-dimensional semidiscrete map and the Jury criterion (stability, and bifurcation type: Neimark–Sacker vs. Flip).

In this paper, following the piecewise constant arguments method of [11], we have semidiscretized the $d = 0$ pine wilt delayed model (1.2) into the two-dimensional system (2.8) for the Ricker recruitment function and into the system (4.2) for the Beverton–Holt recruitment function, and we have carried out the complete equilibrium, stability and bifurcation analysis of both systems. The main conclusions are as follows:

(1) *Methodological results common to both models.* Because the birth term $e^{-\delta\tau} f(w(t-\tau))$ depends only on the delayed state, it cannot be composed into a pure per-capita exponential factor; it must be treated as a constant source term and integrated exactly by the integrating-factor scheme (2.6), which is explicit and positivity-preserving.

(2) *Ricker model.* The existence and local stability of the positive fixed point E_+ are completely characterized by Theorems 3.1 and 3.5; the Jury criterion (3.6) gives a complete stability condition, and $P(-1) > 0$ holds identically, so a period-doubling bifurcation cannot occur in this model. Taking the delay τ as the bifurcation parameter, E_+ undergoes a Neimark–Sacker bifurcation at $\tau^* \approx 1.141$ (Theorem 3.6); by a center manifold reduction, we compute the first Lyapunov coefficient $l_1 \approx -0.052 < 0$, which shows that the bifurcation is supercritical (Theorem 3.7): An asymptotically stable invariant closed curve bifurcates, with amplitude growing as $2.22\sqrt{\tau - \tau^*}$.

(3) *Beverton–Holt model.* The positive fixed point exists if and only if $R_0 > 1$ ($\tau < \tau_0 \approx 26.74$) and is unique (Theorem 4.1). The negative-determinant theorem (Theorem 4.3) shows that $\det J < 0$ at every positive fixed point, so the eigenvalues are always real with opposite signs, and a Neimark–Sacker bifurcation is structurally impossible (Corollary 4.4). The unique destabilization mechanism is a supercritical period-doubling bifurcation at $\tau^*_{\text{flip}} \approx 22.7304$ (Theorem 4.5), producing a stable period-two orbit with amplitude $0.311\sqrt{\tau - \tau^*_{\text{flip}}}$; for large delay, the period-two orbit becomes pulse-like, and it dies out together with the positive fixed point at the transcritical boundary τ_0.

(4) *Numerical verification.* Extensive numerical simulations for both models verify all theoretical predictions, with at least three representative values of the delay τ for each model (Sections 3.8

and 4.8); in particular, the maximal Lyapunov exponent remains nonpositive throughout, so the dynamics is quasiperiodic (Ricker) or period-two (Beverton–Holt), and chaos is absent in both models.

(5) *Discretization effect.* For the Ricker model, the piecewise-constant-arguments semidiscretization shifts the destabilization threshold earlier by about a half ($\tau^* \approx 1.14$ versus $\tau_H^0 \approx 2.01$), a discretization effect that should be stated explicitly.

(6) *Global boundedness and single-attractor property.* Consistent with the global dynamics established for the continuous model by Shu et al. [10], all orbits of the semidiscrete map remain bounded and converge to a unique attractor (equilibrium, invariant closed curve, or period-two cycle) from every initial condition (Section 5, Figure 30); no second attractor and no chaotic regime are observed.

(7) *Biological guidance.* The recruitment function is not a modeling detail: It determines the entire bifurcation structure (overcompensation → Neimark–Sacker; compensation → period-doubling) and the destabilization delay (differing by a factor of about 20). Section 5 gives five practical guidelines (G1)–(G5) for selecting the appropriate recruitment function and for interpreting outbreak data.

Author contributions

Mi Wang: Conceptualization, Methodology, Formal analysis, Software, Writing–original draft; Wenlong Song: Supervision, Validation, Project administration, Writing–review and editing, Funding acquisition. All authors have read and approved the final version of the manuscript for publication.

Use of Generative-AI tools declaration

The authors declare that they have not used Artificial Intelligence (AI) tools in the creation of this article.

Acknowledgments

This work was partially supported by the Fundamental Research Funds for the Central Universities: 60201523050, 2572026DG07.

Conflict of interest

All authors declare no conflicts of interest in this paper.

References

1. K. Futai, Pine wood nematode, bursaphelenchus xylophilus, *Annu. Rev. Phytopathol.*, **51** (2013), 61–83. https://doi.org/10.1146/annurev-phyto-081211-172910

2. J. T. Jones, M. Moens, M. Mota, H. M. Li, T. Kikuchi, Bursaphelenchus xylophilus: opportunities in comparative genomics and molecular host-parasite interactions, *Mol. Plant Pathol.*, **9** (2008), 357–368. https://doi.org/10.1111/j.1364-3703.2007.00461.x

3. B. G. Zhao, K. Futai, J. R. Sutherland, Y. Takeuchi , *Pine wilt disease*, Tokyo: Springer, 2008. https://doi.org/10.1007/978-4-431-75655-2

4. C. Robinet, A. Roques, H. Y. Pan, G. F. Fang, J. R. Ye, Y. Z. Zhang, Role of human-mediated dispersal in the spread of the pinewood nematode in China, *PLoS ONE*, **4** (2009), e4646. https://doi.org/10.1371/journal.pone.0004646

5. M. M. Mota, H. Braasch, M. A. Bravo, A. C. Penas, W. Burgermeister, K. Prager, First report of Bursaphelenchus xylophilus in Portugal and in Europe, *Nematology*, **1** (1999), 727–734. https://doi.org/10.1163/156854199508757

6. T. Soliman, M. C. M. Mourits, W. van der Werf, G. M. Hengeveld, C. Robinet, A. G. J. M. O. Lansink, Framework for modelling economic impacts of invasive species, applied to pine wood nematode in Europe, *PLoS ONE*, **7** (2012), e45505. https://doi.org/10.1371/journal.pone.0045505

7. F. Takasu, Individual-based modeling of the spread of pine wilt disease: vector beetle dispersal and the Allee effect, *Popul. Ecol.*, **51** (2009), 399–409. https://doi.org/10.1007/s10144-009-0145-5

8. Y. Kuang, *Delay differential equations with applications in population dynamics*, Boston: Academic Press, 1993.

9. L. Fonseca, H. Silva, J. M. S. Cardoso, I. Esteves, C. Maleita, S. Lopes, Bursaphelenchus xylophilus in Pinus sylvestris–The first report in Europe, *Forests*, **15** (2024), 1556. https://doi.org/10.3390/f15091556

10. H. Y. Shu, W. X. Xu, X.-S. Wang, J. H. Wu, Spatiotemporal patterns of a structured spruce budworm diffusive model, *J. Differ. Equations*, **336** (2022), 427–455. https://doi.org/10.1016/j.jde.2022.07.014

11. C. Wang, X. Y. Li, Stability and Neimark-Sacker bifurcation of a semi-discrete population model, *J. Appl. Anal. Comput.*, **4** (2014), 419–435. https://doi.org/10.11948/2014024

12. H. Y. Shu, G. H. Fan, H. P. Zhu, Global Hopf bifurcation and dynamics of a stage-structured model with delays for tick population, *J. Differ. Equations*, **284** (2021), 1–22. https://doi.org/10.1016/j.jde.2021.02.037

13. V. G. Nazarenko, Influence of delay on auto-oscillations in cell populations, *Biofizika*, **21** (1976), 352–356.

14. C. S. Holling, The components of predation as revealed by a study of small-mammal predation of the European pine sawfly, *Can. Entomol.*, **91** (1959), 293–320. https://doi.org/10.4039/ent91293-5

15. W. E. Ricker, Stock and recruitment, *Journal of the Fisheries Board of Canada*, **11** (1954), 559–623. https://doi.org/10.1139/f54-039

16. D. Ludwig, D. D. Jones, C. S. Holling, Qualitative analysis of insect outbreak systems: the spruce budworm and forest, *J. Anim. Ecol.*, **47** (1978), 315–332. https://doi.org/10.2307/3939

17. R. J. H. Beverton, S. J. Holt, *On the dynamics of exploited fish populations*, London: Her Majesty's Stationery Office, 1957.

18. J. K. Hale, S. M. V. Lunel, *Introduction to functional differential equations*, New York: Springer, 1993. https://doi.org/10.1007/978-1-4612-4342-7

19. R. M. May, Simple mathematical models with very complicated dynamics, *Nature*, **261** (1976), 459–467. https://doi.org/10.1038/261459a0

20. S. N. Elaydi, *An introduction to difference equations*, 2 Eds., New York: Springer, 1999. https://doi.org/10.1007/978-1-4757-3110-1

21. R. P. Agarwal, *Difference equations and inequalities: theory, methods and applications*, Boca Raton: CRC Press, 2000. https://doi.org/10.1201/9781420027020

22. J. D. Murray, *Mathematical biology*, Heidelberg: Springer, 1989. https://doi.org/10.1007/978-3-662-08539-4

23. E. Liz, A sharp global stability result for a discrete population model, *J. Math. Anal. Appl.*, **330** (2007), 740–743. https://doi.org/10.1016/j.jmaa.2006.06.030

24. S. H. Saker, Periodic solutions, oscillation and attractivity of discrete nonlinear delay population model, *Math. Comput. Model.*, **47** (2008), 278–297. https://doi.org/10.1016/j.mcm.2007.04.007

25. Y. G. Li, Dynamics of a discrete food-limited population model with time delay, *Appl. Math. Comput.*, **218** (2012), 6954–6962. https://doi.org/10.1016/j.amc.2011.12.075

26. T. H. Li, X. T. Zhang, C. R. Zhang, Pattern dynamics analysis of a space-time discrete spruce budworm model, *Chaos Soliton. Fract.*, **179** (2024), 114423. https://doi.org/10.1016/j.chaos.2023.114423

27. K. L. Cooke, J. Wiener, Retarded differential equations with piecewise constant delays, *J. Math. Anal. Appl.*, **99** (1984), 265–297. https://doi.org/10.1016/0022-247x(84)90248-8

28. J. Wiener, *Generalized solutions of functional-differential equations*, Singapore: World Scientific, 1993.

29. W. Li, X. Y. Li, Neimark–Sacker bifurcation of a semi-discrete hematopoiesis model, *J. Appl. Anal. Comput.*, **8** (2018), 1679–1693. https://doi.org/10.11948/2018.1679

30. T. H. Li, X. T. Zhang, M. Wang, C. R. Zhang, Carbon dioxide concentration prediction and optimal control based on coupling with population and greenbelt, *Discrete Cont. Dyn.-B*, **30** (2025), 3180–3205. https://doi.org/10.3934/dcdsb.2025014

31. W. Li, C. R. Zhang, M. Wang, Analysis of the dynamical properties of discrete predator-prey systems with fear effects and refuges, *Discrete Dyn. Nat. Soc.*, **2024** (2024), 9185585. https://doi.org/10.1155/2024/9185585

32. Y. A. Kuznetsov, *Elements of applied bifurcation theory*, 2 Eds., New York: Springer, 1998. https://doi.org/10.1007/b98848

33. S. Wiggins, *Introduction to applied nonlinear dynamical systems and chaos*, 2 Eds., New York: Springer, 2003. https://doi.org/10.1007/b97481

34. B. D. Hassard, N. D. Kazarinoff, Y.-H. Wan, *Theory and applications of Hopf bifurcation*, Cambridge: Cambridge University Press, 1981.

35. J. Carr, *Applications of centre manifold theory*, New York: Springer, 1982. https://doi.org/10.1007/978-1-4612-5929-9

36. J. Guckenheimer, P. Holmes, *Nonlinear oscillations, dynamical systems and bifurcations of vector fields*, New York: Springer, 1983. https://doi.org/10.1007/978-1-4612-1140-2

37. G. Benettin, L. Galgani, A. Giorgilli, J.-M. Strelcyn, Lyapunov characteristic exponents for smooth dynamical systems and for Hamiltonian systems; a method for computing all of them, Part 1: Theory, *Meccanica*, **15** (1980), 9–20. https://doi.org/10.1007/bf02128236

38. C. Robinson, *Dynamical systems: stability, symbolic dynamics, and chaos*, 2 Eds., Boca Raton: CRC Press, 1998. https://doi.org/10.1201/9781482227871

A. Taylor expansion coefficients

In the notation of (3.1) and (3.3), the nonzero coefficients in (3.13) are

$$\begin{aligned} a_{20} &= -\frac{1}{2}\frac{\partial^2 A}{\partial v^2}\Big|_{E_+} w^* \mathrm{e}^A + \frac{1}{2}\Big[\frac{\partial^2 C}{\partial u^2}\frac{\mathrm{e}^A - 1}{A}\Big]\Big|_{E_+}, \\ a_{11} &= -\frac{\partial A}{\partial v}\Big|_{E_+} w^* \mathrm{e}^A, \qquad a_{30} = -\frac{1}{6}\frac{\partial^3 A}{\partial v^3}\Big|_{E_+} w^* \mathrm{e}^A + \cdots, \end{aligned} \tag{A.1}$$

where

$$\frac{\partial A}{\partial v} = -\tau\frac{1-y^2}{(1+y^2)^2}, \quad \frac{\partial^2 A}{\partial v^2} = -\tau\frac{2y(y^2-3)}{(1+y^2)^3}, \quad \frac{\partial^3 A}{\partial v^3} = -\tau\frac{6(1-6y^2+y^4)}{(1+y^2)^4},$$

$$\frac{\partial C}{\partial u} = \tau \mathrm{e}^{-\delta\tau} b \mathrm{e}^{-au}(1-au), \quad \frac{\partial^2 C}{\partial u^2} = -\tau \mathrm{e}^{-\delta\tau} ab \mathrm{e}^{-au}(2-au), \quad \frac{\partial^3 C}{\partial u^3} = \tau \mathrm{e}^{-\delta\tau} a^2 b \mathrm{e}^{-au}(3-au),$$

all evaluated at E_+ ($u = w^*$, $v = w^*$). The third-order coefficients a_{21}, a_{12}, a_{03} are obtained from the combinations (after symmetrization) of $\frac{\partial^3 A}{\partial v^3}$ and $\frac{\partial^3 C}{\partial u^3}$. All the first Lyapunov coefficient computations are carried out by symbolic differentiation with sympy to ensure accuracy.

AIMS Press

© 2026 the Author(s), licensee AIMS Press. This is an open access article distributed under the terms of the Creative Commons Attribution License (https://creativecommons.org/licenses/by/4.0)